A benchmark comparison of spontaneous subduction models—Towards a free surface

H. Schmeling [a,*], A.Y. Babeyko [a,b], A. Enns [a], C. Faccenna [c], F. Funiciello [c], T. Gerya [d], G.J. Golabek [a,d], S. Grigull [a,e], B.J.P. Kaus [d,g], G. Morra [c,d], S.M. Schmalholz [f], J. van Hunen [h]

[a] Goethe University, Institute of Earth Sciences, Altenhöferallee 1, 60438 Frankfurt, Germany
[b] Deutsches GeoForschungsZentrum, Telegrafenberg, 14473 Potsdam, Germany
[c] Dip. Scienze Geologiche, Università degli Studi "Roma TRE", Largo S.Leonardo Murialdo 1, 00146 Roma, Italy
[d] Geophysical Fluid Dynamics Group, Institute of Geophysics, Department of Geosciences, Swiss Federal Institute of Technology (ETH-Zurich), CH-8093 Zurich, Switzerland
[e] School of Geography, Environment and Earth Sciences (SGEES), Victoria University of Wellington, PO Box 600, Wellington, New Zealand
[f] Geological Institute, ETH Zurich, Leonhardstrasse 19, 8092 Zurich, Switzerland
[g] Department of Earth Sciences, University of Southern California, 3651 Trousdale Parkway, Los Angeles, CA 90089-740, USA
[h] Durham University, Department of Earth Sciences, Science Site, Durham DH1 3LE, United Kingdom

ARTICLE INFO

ABSTRACT

Numerically modelling the dynamics of a self-consistently subducting lithosphere is a challenging task because of the decoupling problems of the slab from the free surface. We address this problem with a benchmark comparison between various numerical codes (Eulerian and Lagrangian, Finite Element and Finite Difference, with and without markers) as well as a laboratory experiment. The benchmark test consists of three prescribed setups of viscous flow, driven by compositional buoyancy, and with a low viscosity, zero-density top layer to approximate a free surface. Alternatively, a fully free surface is assumed. Our results with a weak top layer indicate that the convergence of the subduction behaviour with increasing resolution strongly depends on the averaging scheme for viscosity near moving rheological boundaries. Harmonic means result in fastest subduction, arithmetic means produces slow subduction and geometric mean results in intermediate behaviour. A few cases with the infinite norm scheme have been tested and result in convergence behaviour between that of arithmetic and geometric averaging. Satisfactory convergence of results is only reached in one case with a very strong slab, while for the other cases complete convergence appears mostly beyond presently feasible grid resolution. Analysing the behaviour of the weak zero-density top layer reveals that this problem is caused by the entrainment of the weak material into a lubrication layer on top of the subducting slab whose thickness turns out to be smaller than even the finest grid resolution. Agreement between the free surface runs and the weak top layer models is satisfactory only if both approaches use high resolution. Comparison of numerical models with a free surface laboratory experiment shows that (1) Lagrangian-based free surface numerical models can closely reproduce the laboratory experiments provided that sufficient numerical resolution is employed and (2) Eulerian-based codes with a weak surface layer reproduce the experiment if harmonic or geometric averaging of viscosity is used. The harmonic mean is also preferred if circular high viscosity bodies with or without a lubrication layer are considered. We conclude that modelling the free surface of subduction by a weak zero-density layer gives good results for highest resolutions, but otherwise care has to be taken in (1) handling the associated entrainment and formation of a lubrication layer and (2) choosing the appropriate averaging scheme for viscosity at rheological boundaries.

© 2008 Elsevier B.V. All rights reserved.

1. Introduction

While dynamically modelling of subduction has been an issue in the geodynamical literature since a long time (e.g. Jacoby, 1976; Jacoby and Schmeling, 1982) only recently a vast number of numerical and laboratory models have been developed in an attempt to understand the dynamics of self-consistently forming subduction zones (Bellahsen et al., 2005; Funiciello et al., 2003a,b; Schmeling

* Corresponding author. Tel.: +49 69 798 40128; fax: +49 69 798 40131.
E-mail addresses: schmeling@geophysik.uni-frankfurt.de (H. Schmeling),
faccenna@uniroma3.it (C. Faccenna), ffunicie@uniroma3.it (F. Funiciello),
taras.gerya@erdw.ethz.ch (T. Gerya), kaus@erdw.ethz.ch (B.J.P. Kaus),
schmalholz@erdw.ethz.ch (S.M. Schmalholz), jeroen.van-hunen@durham.ac.uk
(J. van Hunen).

et al., 1999; Tetzlaff and Schmeling, 2000; Capitanio et al., 2007, and others). The term "self-consistent" emphasizes that the formation of the trench and the sinking of the slab is driven by internal forces only and without invoking prescribed zones of weakness. One of the major problems in all models is to formulate and apply a method to decouple the subducting slab from the surface or the overriding plate. While early modellers simply assumed a sufficiently large region near the trench in which the mantle was artificially weakened, other models invoked more complex rheologies or neglected the overriding plate at all (Schmeling and Jacoby, 1981; Becker et al., 1999; Funiciello et al., 2004, 2006; Kincaid and Olson, 1987; Martinod et al., 2005; Schellart et al., 2004a,b, 2005; Stegman et al., 2006).

Laboratory models have the possibility to simulate realistic geologic features using complex rheologies and at the same time having the advantage of an intrinsically 3D approach. However, 3D aspects are often suppressed using laterally homogeneous slabs affected by box boundary effects (Kincaid and Olson, 1987; Shemenda and Grocholsky, 1992) or by using 2D feeding pipes to inject the slab into a density/viscosity layered fluid (Griffiths and Turner, 1988; Griffiths et al., 1995; Guillou-Frottier et al., 1995). 3D laboratory models including lateral slab migration have been recently realized prescribing kinematically the trench movement by Buttles and Olson (1998) and Kincaid and Griffiths (2003) and dynamically self-consistently by Faccenna et al. (2001) and Funiciello et al. (2003a,b, 2004, 2006) and Schellart (2004a,b, 2005). 3D numerical subduction models have been studied, e.g. by Stegman et al. (2006) and Schellart et al. (2007).

All these approaches can be divided into two classes: In one class subduction is kinematically or rheologically prescribed by kinematic boundary conditions of weak decoupling zones. In the other class the decoupling zones evolves self-consistently. Our benchmark addresses this second class of models. Furthermore our setup studies a slab without an overriding plate. Thus the dynamics reveals the behaviour of a subducting slab as it decouples from the free surface without being influenced by another plate.

Although our benchmark definition might look quite simple, as it describes a purely viscous, isothermal fluid dynamical problem with linear creeping rheology, and the viscosity contrasts are 10^4 at most, it turns out to be a very challenging test. This is because of the decoupling mechanism acting in real systems in which dense bodies detach from a surface, even if they are purely viscous: layers of different composition interact dynamically, are smeared out and turn into lubrication layers. As the numerical resolution of our codes is limited, such fluid dynamical scenarios easily exceed the limitations of even high resolution runs. To explore how these limits are reached by different codes and what can be done to tackle these resolution problems is one of the motivations of the present benchmark.

Our approach is threefold. In one set of tests (case 1) we try to benchmark the process of subduction approximating the subduction zone to be overlain by a soft buoyant layer ("sticky air" or an artificial layer whose lowermost part consists of water rich, weak sediments, in short "soft sediments") and compare it to subduction models with a free surface. As it will turn out, the soft material will be entrained, lubricating the subducting slab, and the subducting slab is decoupled from the overriding mantle in a self-consistent way. However, the lubricating layer will be very thin, its thickness is beyond the resolution of our models. Consequently, to achieve convergence of the different codes will be difficult. Notwithstanding, such model approaches are frequently discussed in the literature. Therefore, it is interesting to study how the different methods deal with this decoupling/lubricating problem, how the algorithms of determining the effective viscosity at the lubrication region han-

dle the problem, and how they compare to models with a free surface.

In a second approach (case 2), an attempt is made to achieve convergent results of the different codes. We will define a modified setup, namely one without the formation of a thin lubricating layer. In this setup, the viscosity of the overlying layer will be chosen as equal to the mantle viscosity. Consequently, no lubrication layer can form, and one should expect that the resulting evolution of subduction should converge among the different codes. It should be emphasized, that we do not suggest this setup to be realistic in the sense of subduction dynamics, but it is a reasonable fluid dynamic setup to test codes which model the evolution of a triple point associated with a subduction zone. For constant viscosity thermal convection the role of such a triple point on entrainment of material with a different density has already been benchmarked by van Keken et al. (1997).

Thirdly (case 3), we benchmark a laboratory subduction model with a free surface and try to reproduce it as close as possible by numerical models with a weak top layer or with free surface numerical models.

In Section 5, we present a well-resolved case of a Stokes flow problem with and without a lubrication layer to test the applicability of our algorithms of determining the effective viscosity near compositional rheological boundaries.

2. Definition of cases

2.1. Governing equations

The benchmark is defined as a purely viscous fluid dynamic problem. We assume an incompressible fluid, in which driving density fields are advected with the flow. Then the problem can be described by the equations of conservation of mass

$$\vec{\nabla} \cdot \vec{v} = 0 \tag{1}$$

and the equation of momentum

$$-\vec{\nabla}P + \frac{\partial}{\partial x_j}\left[\eta_k\left(\frac{\partial v_i}{\partial x_j} + \frac{\partial v_j}{\partial x_i}\right)\right] - \rho_k g \vec{e}_3 = 0 \tag{2}$$

where $\vec{v}$ is the velocity, P the pressure, x the coordinates, η_k the viscosity of composition k, ρ_k the density of composition k, g gravity acceleration, and $\vec{e}_3$ the unit vector in vertical upward direction. The viscosity and the density are advected with the flow. The corresponding advection equation is given by

$$\frac{\partial C_k}{\partial t} + \vec{v} \cdot \vec{\nabla}C_k = 0 \tag{3}$$

where C_k is the concentration of the k-th composition. C_k is equal to 1 in a region occupied by composition k and 0 elsewhere.

2.2. Model setup

The 2D model setup for cases 1 and 2 is shown in Fig. 1. It is defined by a layer of 750 km thickness and 3000 km width. The initial condition is specified by a mantle of 700 km thickness, overlain by a 50 km thick soft surface layer mimicking "sticky air" or "soft sediments". The mantle layer consists of a highly viscous, dense lithosphere ($\rho_l = 3300$ kg/m^3, $\eta_l = 10^{23}$ Pa s, initial thickness of 100 km) and an ambient mantle with $\rho_m = 3200$ kg/m^3, $\eta_m = 10^{21}$ Pa s. The surface layer of initially 50 km thickness has a density $\rho_s = 0$ kg/m^3 and a viscosity of either $\eta_s = 10^{19}$ Pa s or $\eta_s = 10^{21}$ Pa s and a free slip top. In order to trigger subduction and mechanical decoupling of the slab from the surface in a most direct and simple way the slab tip is already penetrating into the mantle
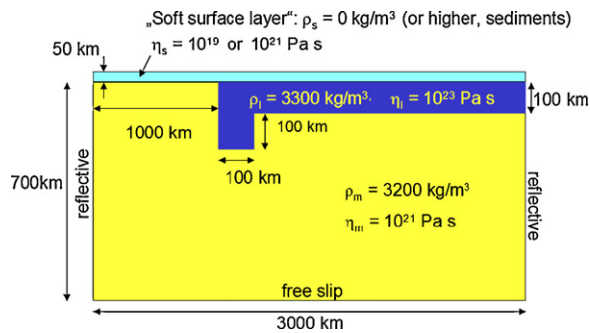
Fig. 1. Model setup and initial condition of the benchmark cases 1 and 2.

as deep as 200 km (from the top of the mantle). This configuration with a 90° corner avoids that time-dependent bending might mask the detachment of the slab from the surface. The mechanical boundary conditions are reflective (free slip), implying the slab being attached to the right boundary.

The model setup for the free surface case is identical to the setup described above, only the weak surface layer is removed, and the surface boundary condition is free.

The model setup for the laboratory experiments and the corresponding numerical experiments (case 3) is somewhat different and will be described in detail in Section 3.3.

3. Methods

3.1. The participating codes

3.1.1. FDCON

The code FDCON (used by authors Schmeling, Golabek, Enns, and Grigull) is a finite difference code. Eqs. (1) and (2) are rewritten as the biharmonic equation in terms of the stream function and variable viscosity (e.g. Schmeling and Marquart, 1991). The FD formulation of the biharmonic equation results in a symmetric system of linear equations, which is directly solved by Cholesky decomposition. The advection equation is solved by a marker approach (e.g. Weinberg and Schmeling, 1992). The region is filled completely with markers which carry the information of composition k. The concentration C_k of composition k at any FD grid point is determined by the number of markers of composition k found within a FD-cell sized area around the grid point divided by the total number of markers present in the same cell. The density and viscosity at any grid point are determined by C_k—weighted averaging using either the harmonic, the geometric or the arithmetic mean (see below). The markers are advanced by a 4th order Runge-Kutta scheme, combined with a predictor–corrector step. For this predictor-corrector step, markers are provisionally advanced by two first order Eulerian steps. The Navier Stokes equation is solved for these preliminary steps to obtain the corresponding velocity fields. These velocity fields are then taken for the full 4th order Runge-Kutta step to advance the markers.

3.1.2. I2VIS, I2ELVIS

Both the viscous code I2VIS (used by author Gerya) and the viscoelastic code I2ELVIS are based on a combination of finite-differences (pressure–velocity formulation on fully staggered grid) with marker-in-cell technique (Gerya and Yuen, 2003a, 2007). Markers carry information on composition (which is used to define density, viscosity and shear modulus) and stresses (in viscoelastic case). Viscosity, density and stresses (in viscoelastic case) are interpolated from markers to nodes by using bilinear distance-

dependent schemes. In I2ELVIS the shear modulus for viscous runs was taken as 6.7×10^{30} Pa and the bulk modulus was taken infinity (incompressible fluid). Obviously with a time step of 10^4 years and a viscosity of the slab of 10^{23} Pa s there is no elastic deformation component. The markers are advanced by a 4-th order in space 1st order in time Runge-Kutta scheme. The runs done with I2ELVIS differ from those with I2VIS in that they average the viscosity around nodes more locally. In I2ELVIS averaging from markers to a node is done from markers found in 1-grid cell around the node (i.e. within 0.5-grid step). Averaging in I2ELVIS is done separately for different nodal points corresponding to shear (interceptions of grid lines) and normal (centres of cells) stress components. In I2VIS averaging from markers to nodes is first uniformly done for nodal points corresponding to shear stress components (i.e. for intersections of grid lines) from markers found in $2 \times 2 = 4$ grid cells around each nodes (i.e. within 1.0 grid step). Then viscosity for normal stress components is computed for centres of cells by averaging viscosity from four surrounding "shear viscosity nodes" (i.e. averaging is effectively from $3 \times 3 = 9$ cells, within 1.5-grid step). Both codes use the optional possibility of refinement locally in a 100–800 km wide and 10–20 km deep area (Swiss-cross-grid following the trench). Therefore, the subsequent models converge better for the initial 10–20 Myears of the model development.

3.1.3. LAPEX-2D

This code (used by author Babeyko) solves for balances of mass, momentum and energy through an explicit Lagrangian finite difference technique (FLAC-type) (Cundall and Board, 1988; Poliakov et al., 1993; Babeyko et al., 2002) combined with particle-in-cell method (Sulsky et al., 1995). The solution proceeds on a moving Lagrangian grid by explicit time integration of conservation equations. For that reason, the inertial term $\rho^{inert} \partial v_i / \partial t$ is included into the right-hand side of the momentum conservation equation (Eq. (2)). Here inertial density ρ^{inert} actually plays a role of parameter of dynamic relaxation. Incorporation of the inertial term allows explicit time integration of nodal velocities and displacement increments, thus "driving" the solution towards quasi-static equilibrium. The magnitude of the inertial term is kept small in comparison to tectonic forces, typically, $10^{-3}–10^{-5}$, so the solution remains quasi-static. In comparison to the classical implicit finite element algorithm, memory requirements of this method are very moderate, since no global matrices are formed and inverted. Accordingly, computational costs for one time step are very low. However, explicit time integration imposes very strict restrictions on the magnitude of the calculational time step—for typical geodynamic application the stable Courant time step has an order of 1–10 years. Being a disadvantage of this method, the small computational time step allows, however, treatment of any physical non-linearity (such as plastic flow, for example) in a natural way, without any additional iterations and problems with convergence. A principal restriction in LAPEX-2D, which partly limited its suitability for the present benchmark setup, is the requirement of non-zero material density. Thus benchmarks with zero-density 'sticky air' soft layer were not performed with LAPEX-2D. The algorithm is easy parallelizable.

LAPEX-2D has a principally viscoelastic solver. The explicit numerical scheme of stress update at each computational time step directly exploits the elastic constitutional law. Thus, elasticity cannot be completely 'switched-off'. In the present models, the slab was assigned the elastic properties of olivine, i.e. Young's modulus $E = 184$ GPa and Poisson's ratio of 0.244. Together with slab viscosity of 10^{23} Pa s these elastic properties correspond to the Maxwell relaxation time of 40 kyears, which is much less than the charac-

teristic model time. Thus, the behaviour of the slab in LAPEX-2D is effectively viscous.

Solution on the moving Lagrangian grid becomes non-accurate when the grid becomes too distorted. At this point remeshing should take place. During remeshing the new grid is built, and solution variables are interpolated from the old distorted grid. This procedure of remeshing is inevitably related to the problem of numerical diffusion. In the case of history-dependent solution, like presence of elastic stresses, and strong stress gradients (e.g. subducting slab vs. its surrounding), uncontrollable numerical diffusion might strongly affect the solution. In order to sustain it, we have implemented in our code a particle-in-cell, or material point technique (Sulsky et al., 1995). In this approach, particles, which are distributed throughout the mesh, are more than simple material tracers. In LAPEX-2D, particles, typically 30–60 per element, track not only material properties but also all history-depending variables including full strain and stress tensors. Between remeshings, particles provide no additional computational costs since they are frozen into the moving Lagrangian grid composed of constant–stress triangles, and there is no need to update particle properties at this stage. Additional computational efforts arise only during remeshing. First, stress and strain increments accumulated since the previous remeshing are mapped from Lagrangian elements to particles. After the new mesh is constructed, stresses and strains are back-projected from particles onto the new grid.

3.1.4. CITCOM

The code CITCOM (used by author van Hunen) is a finite element code (Moresi and Solomatov, 1995; Moresi and Gurnis, 1996; Zhong et al., 2000). The finite elements are bi-linear rectangles, with a linear velocity and a constant pressure. Interpolation of composition is done per element and directly applied to the integration points. The code uses an iterative multigrid solution method for the Stokes equation. Eqs. (1) and (2) in their discrete form are written as

$$Au + Bp = f \tag{4}$$

$$B^{T}u = 0 \tag{5}$$

This system of equations is solved with some form of the Uzawa iteration scheme: Eq. (4) is solved iteratively with a Gauss–Seidel multigrid method, while applying Eq. (5) as a constraint. The augmented Lagrangian formulation is used to improve convergence of the pressure field for large viscosity variations. A marker approach is used to solve the advection Eq. (3): the computational domain is filled completely with markers (approximately 40 markers per finite element), which carry the composition. Markers are advected using a second order Runge-Kutta scheme. Interpolation from the markers onto the integration points of the finite element mesh is done by a geometric weighted average of the marker values over each element (i.e. one value per element).

3.1.5. ABAQUS with remeshing

An adaptive solid mechanical Finite Element Method (Abaqus Standard) (used by author Morra) that uses the tangent operator matrix is employed for calculating the deformation of the mantle. In order to avoid excessive deformation, every 1 Myear a remeshing algorithm re-interpolates the variables to the initial mesh. The materials are traced using a field defined at the nodes (field 1: 0 = air, 1 = mantle; field 2: 0 = mantle, 1 = lithosphere) and the material properties are calculated interpolating the field at the four nodes around each linear quadratic element. Rheology is implemented in all configurations, using geometric, arithmetic and harmonic mean. For the viscous runs the elastic modulus is increased by two orders of magnitude compared to the real value in nature (i.e.

10^{13} Pa vs. 10^{11} Pa), which reduces the Maxwell time by two orders of magnitude, therefore inhibiting elasticity (stresses are dissipated immediately, with virtually no delay).

3.1.6. LaMEM

LaMEM (used by author Kaus) is a thermo-mechanical finite element code that solves the governing equations for Stokes flow in parallel in a 3D domain using Uzawa iterations for incompressibility and direct, iterative or multigrid solvers (based on the PETSc package). A velocity–pressure formulation is employed with either Q_1P_0 (linear) elements or Q_2P_{-1} elements (quadratic for velocity and linear discontinuous for pressure). To facilitate comparison with similar FEM methods in this benchmark study (such as CIT-COM), all computations have been performed with linear elements. Tracers are used to advect material properties as well as stress tensors. Material properties are computed at integration points by arithmetic averaging from the nearest tracers. In free surface runs, the properties at the integration points are employed for calculations. In selected cases, the values from all integration points in an element are homogenized through arithmetic, geometric or harmonic averaging (which thus yields one value of viscosity per cell). Tracer advection is done through mapping of global tracer coordinates to local ones, after which the element is deformed, and tracer locations are mapped back to global coordinates. LaMEM can be employed in an Eulerian mode, in a purely Lagrangian mode, or in an Arbitrary Lagrangian–Eulerian (ALE) mode, in which some elements are deformed (typically close to the free surface) but others are fix. The ALE mode employs remeshing after each time step.

An advantage of LaMEM is that it can handle self-consistent free surface deformation, while simultaneously solving the Stokes equation in an implicit manner. In free surface simulations the ALE approach is used with remeshing based on the free surface deformations. Remeshing is done at each time-step, and a new free surface is created from the old one by linear interpolation on regular *x*-coordinates. If angles larger than 25° occur at the free surface after remeshing, a kinematic redistribution algorithm is employed that distributes the fluid over adjacent nodes in a mass conservative manner (until angles <25°).

3.1.7. FEMS-2D

FEMS-2D (used by author Schmalholz) is a finite element code for simulating slow incompressible flows in two dimensions (Frehner and Schmalholz, 2006; Schmalholz, 2006) and is written in MATLAB (The MathWorks). The algorithm is based on a mixed velocity–pressure formulation (e.g. Hughes, 1987). Two different elements can be used: (i) the isoparametric Q_2–P_1 9-node quadrilateral element using nine integration points, a biquadratic velocity approximation and a linear discontinuous pressure approximation or (ii) the isoparameteric P_2–P_1 7-node triangular element using seven integration points, a quadratic velocity approximation and a linear discontinuous pressure approximation (e.g. Cuvelier et al., 1986; Hughes, 1987; Bathe, 1996). The higher order elements for the velocities are used in combination with linear elements for the pressure. This so-called mixed velocity–pressure formulation is especially accurate for pressure calculations for incompressible flows (which are not calculated using a stream function ansatz). The higher order elements should here not matter concerning the overall accuracy of the calculated flow field. Both elements satisfy the inf-sup condition guaranteeing numerical stability for incompressible flows. Uzawa-type iterations are used to achieve incompressible flow. For both elements the pressure is eliminated on the element level. For the presented numerical subduction simulations the triangular elements are used. The applied mesh generator is Triangle developed by Shewchuk (1996,

www.cs.cmu.edu/∼quake/triangle.html). An algorithm written in MATLAB (developed and provided by Dani Schmid, PGP, University of Oslo, Norway) is used to link the mesh generator Triangle with FEMS-2D. After each time step the coordinates of the nodes are updated by adding the corresponding displacements which result from the product of the calculated velocities times the time step (explicit time integration). The new velocity field is then calculated for the new nodal coordinates.

Recently, the matrix assembly algorithm and solver developed by Dabrowski et al. (2008) was implemented in FEMS-2D which shortened the computation time significantly. This version has been named MILAMIN (used by authors Schmalholz and Kaus). Tests have shown that the results are identical to models with FEMS-2D.

Due to the applied Lagrangian approach the numerical mesh is deformed with the calculated velocities. When the finite element triangles are too strongly deformed, the finite element mesh is remeshed but the contour lines defining the geometry of the mantle and the slab remain unchanged. There is also one point at the free surface at which the mantle surface and the slab surface are identical, i.e. the point defining the trench. During the slab subduction the mantle is overriding the slab and the contour line defining the free surface of the mantle gets overturned, which is unrealistic. Therefore, once the mantle surface exceeds a critical angle (between 10 and 90°), the trench point is moved upwards along the contour line defining the slab surface. Two different approaches have been applied: in the first approach the trench point is simply moved upwards to the next nodal point on the contour line of the slab surface and the mantle surface is additionally smoothed. This approach does not guarantee a strict mass conservation. In the second approach, a new trench point is generated at the slab surface so that the surface of the mantle exhibits a predefined angle at the trench (here 10°) and additionally the mass of mantle material is conserved. It was found that when the numerical resolution is sufficiently large (i.e. the results of each algorithm do not change significantly anymore with higher resolution) around the trench, both approaches yield nearly identical results. The stepwise change of the trench location caused by the adjustment of the contour lines can be physically interpreted with some kind of stick–slip behaviour, where stresses first build up and are then released by the slip of mantle material along the surface of the slab.

3.2. Viscosity averaging

At compositional boundaries all codes have the problem of either to map the viscosity (and density) advected by the markers to the FD- or FE grid, or to interpolate viscosities from a deformed mesh to a remeshed configuration. This is done by using either of the following averaging laws:

Harmonic mean:

$$\frac{1}{\eta_{ave}} = \frac{C_1}{\eta_1} + \frac{C_2}{\eta_2} \tag{6}$$

Arithmetic mean:

$$\eta_{ave} = C_1\eta_1 + C_2\eta_2 \tag{7}$$

Geometric mean:

$$\eta_{ave} = \eta_1^{C_1}\eta_2^{C_2} \tag{8}$$

Here η_i is the viscosity of composition i, and C_i is the relative volumetric fraction of composition i in the vicinity of the FE- or FD-node at which the effective viscosity η_{ave} is needed. A physical discussion of the above laws will be presented below.

Another viscosity averaging scheme which deliberately avoids any a priori assumptions about the averaging process, or any information about marker distributions on a scale below the grid resolution is the "infinite norm average":

$$\eta_{ave} = \eta_k, \quad \text{with } k: \ C_k \geq C_i, \quad i = 1, \ldots, n_{mat} \tag{9}$$

where n_{mat} is the total number of compositions. Eq. (9) simply states that the material which has most particles in a cell determines the material properties of that cell.

In the subsequent sections, we essentially use and compare models with the harmonic, arithmetic and geometric means, and apply the infinite norm average only in one resolution test. In Section 5, the infinite norm scheme is discussed and quantified for a 2D-Stokes flow problem.

3.3. Laboratory experiments and setup of corresponding numerical runs

We (authors Funiciello and Faccenna) use silicone putty (Rhodrosil Gomme, PBDMS + iron fillers) and glucose syrup as analogue of the lithosphere and upper mantle, respectively. Silicone putty is a viscoelastic material behaving viscously at experimental strain rates (Weijermars and Schmeling, 1986) since the deformation time-scale is always larger than its Maxwell relaxation time (about 1 s). Glucose syrup is a transparent Newtonian low-viscosity fluid. These materials have been selected to achieve the standard scaling procedure for stresses scaled down for length, density and viscosity in a natural gravity field ($g_{model} = g_{nature}$) as described by Weijermars and Schmeling (1986) and Davy and Cobbold (1991).

The layered system, where densities and viscosities are assumed as constant over the thickness of the individual layers, is arranged in a transparent Plexiglas tank (Fig. 2a). The subducting plate is fixed to the box in the far field ("fixed ridge" see Kincaid and Olson, 1987). 3D natural aspects of laboratory models are minimized using slabs as large as the width of the box ($w = b$). It allows to consider in first approximation the system as two-dimensional for comparison with the numerical models of the present benchmark. The box sides are lubricated with Vaseline to avoid sticking effects of the slab with the box boundaries.

The subduction process is manually started by forcing downward the leading edge of the silicone plate into the glucose to a depth of 3.1 cm (corresponding to about 200 km in nature) at an angle of ∼30°. In Fig. 2a and Table 1 we summarized the characteristics of the selected experiment we describe in the present paper. For more detailed explanations see Funiciello et al. (2003a,b, 2004). The experiment is monitored over its entire duration by two digital cameras both in the lateral and top views. Kinematic and geometric parameters (trench retreat, dip of the slab) are afterwards quantified by means of image analysis tools

Table 1
Parameters of the laboratory experiment (case 3)

Parameter	Value
Gravity acceleration (m s^{-2})	9.81
Thickness (m)	
$\quad h$, oceanic lithosphere	0.012
$\quad H$, upper mantle	0.103
Density (kg m^{-3})	
$\quad \rho_o$, oceanic lithosphere	1495
$\quad \rho_m$, upper mantle	1415
$\quad$ Density contrast, $\rho_o - \rho_m$	80
Viscosity (Pa s)	
$\quad \eta_o$, oceanic lithosphere	3.5×10^5 (±5%)
$\quad \eta_m$, upper mantle	32 (±20%)
$\quad$ Viscosity ratio, η_o/η_m	1.1×10^4
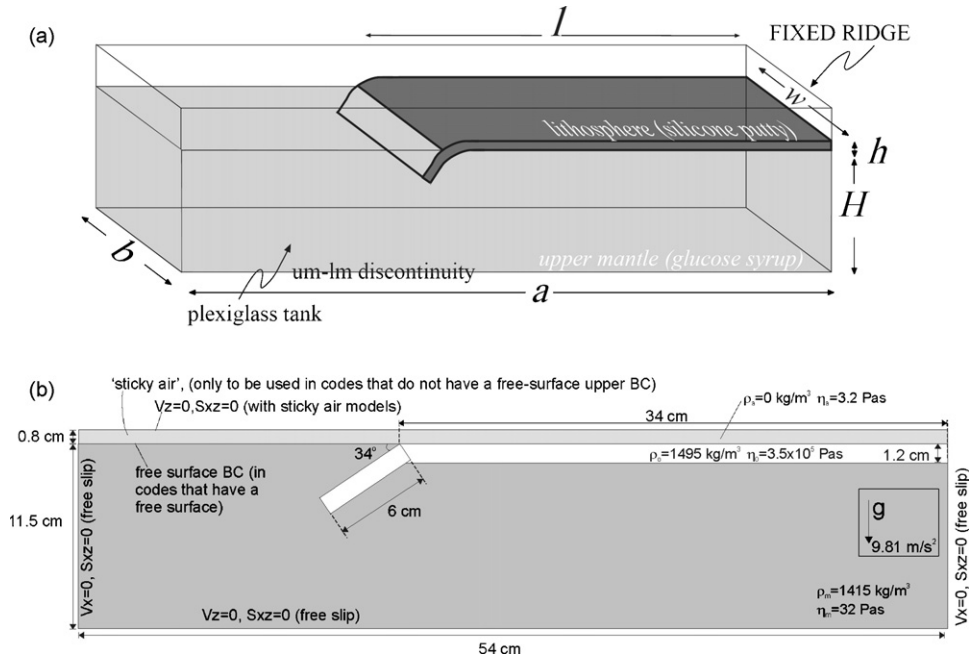
Fig. 2. (a) Experimental setup of the subduction benchmark case 3. $a = 54$ cm, $b = 25$ cm, $l = 40$ cm (=34 cm along surface, 6 cm dipping), $w = 25$ cm, $h = 1.2$ cm, $H = 10.3$ cm. (b) Setup for the corresponding numerical models.

Table 2
Case 1 models, i.e. models with weak surface layer, $\rho_s = 0$ kg/m^3, $\eta_s = 10^{19}$ Pa s

Model name	Number of nodes (local trench area resolution in km)	No. of markers	Averaging method	Remarks
FDCON-1	161 × 41	1800 × 450	Geom	$dt = 0.01$ Courant in all FDCON runs
FDCON-2	241 × 61	2700 × 675	Geom	
FDCON-3	321 × 81	3600 × 900	Geom	
FDCON-4	561 × 141	6250 × 1570	Geom	
FDCON-5	561 × 141	6250 × 1570	Harm	
FDCON-6	561 × 141	6250 × 1570	Arith	
I2VIS	301 × 76 (10 × 1 km)	801,700	Arith, geom, harm	Local grid refinement, $dt = 10$ kyears
	381 × 76 (5 × 1 km)	812,560		
	621 × 76 (2 × 1 km)	994,620		
	1021 × 76 (1 × 1 km)	1,091,080		
	1821 × 93 (0.5 × 0.5 km)	356,512		
I2ELVIS	301 × 76 (10 × 1 km)	952,500	Arith, geom, harm	Local grid refinement, $dt = 10$ kyears
	381 × 76 (5 × 1 km)	988,000		
	621 × 76 (2 × 1 km)	1,255,500		
	1021 × 76 (1 × 1 km)	1,479,000		
	1821 × 93 (0.5 × 0.5 km)	3,835,740		
	884 × 125 (0.2 × 0.2 km)	7,473,712		
I2ELVIS	161 × 41		Arith, geom, harm	Uniform grid, $dt = 10$ kyears
	241 × 61			
	301 × 76			
	321 × 81			
	561 × 141			
CITCOM-1	128 × 32		Geom	$dt = 0.01$ Courant
CITCOM-2	256 × 64		Geom	$dt = 0.01$ Courant
LAPEX2D-1	150 × 38		Geom	$\eta_s = 10^{20}$ Pa s, $dt = 10$–20 years
LAPEX2D-2	300 × 75		Geom	$\eta_s = 10^{20}$ Pa s, dt as above
LAPEX2D-3				Free surface, dt as above
LaMEM-1	64 × 16 × 2	65,536	None	Free surface, $dt = 10$ kyears (40 sub-time steps per time step)
LaMEM-2	128 × 32 × 2	884,736	None	Free surface, dt as above
LaMEM-3	256 × 64 × 2	1,048,576	None	Free surface, dt as above
FEMS-2D-1	2850 nodes (equivalent to 111 × 26 irregular nodes with local refinement)	Marker chain	None	Free surface, $dt = 2$ kyears
FEMS-2D-2	5000, equ 146 × 34 irr., l.r.	Marker chain	None	Free surface, $dt = 1$ kyear
FEMS-2D-3	15000, equ 256 × 59 irr., l.r.	Marker chain	None	Free surface, $dt = 1$ kyear

(software DIAna Image Analysis). The measurement error was ±0.1 cm.

The laboratory setup is taken to define a corresponding 2D numerical setup (Fig. 2b). As these experiments are carried out by both the codes with a free surface and with a soft surface layer ("sticky air"), both alternative setups are depicted in Fig. 2b. Based on the photograph of the laboratory model at time equal zero, the initial dip angle and length of the leading edge of the slab are chosen as 34° and 6 cm, respectively.

4. Results

We first present results of case 1 with a weak decoupling layer (10^{19} Pa s), which leads to the entrainment of weak material and effective lubrication of the upper side of the subducting slab. We then show the results of the free surface runs. This will be followed by the non-lubrication models (case 2) with a "weak layer" of 10^{21} Pa s. Finally (case 3) the laboratory result and the corresponding numerical runs will be shown.

4.1. Models with weak decoupling layer (case 1)

These models have been run with different resolutions by the codes and are summarized in Table 2. The typical behaviour of a case 1 model is shown in Fig. 3. At time 0 instantaneously high vertical flow velocities of the order of 5.4 cm/a are observed as the originally flat mantle/lithosphere surface relaxes towards an isostatic equilibrium. This equilibrium is approached after about 100–200 kyears, and is associated with a vertical offset at the trench of about 4 km. This isostatic relaxation is confirmed by the codes FDCON (3.8 km after 180 kyears), CITCOM (3.9 km after 183 kyears), I2ELVIS (4.7 km
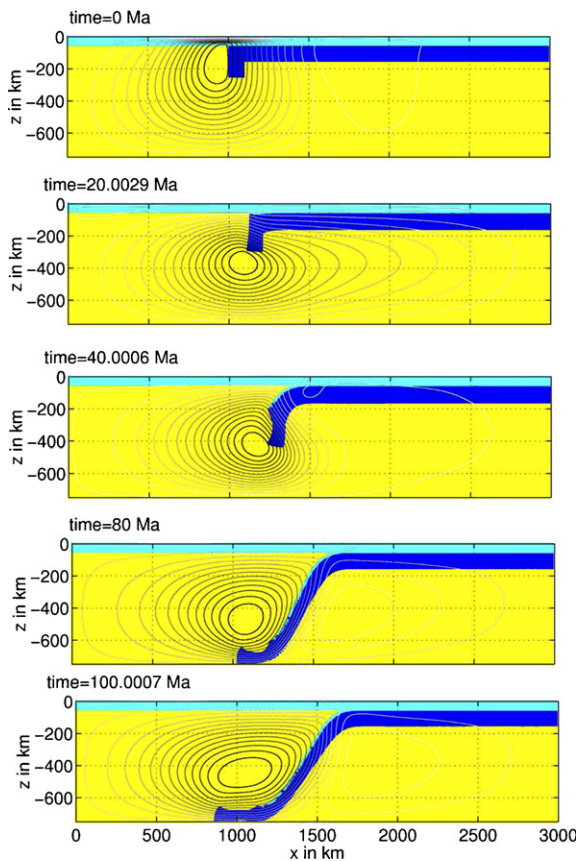
after 400 kyears) with an accuracy of approximately 100 m, as well as by the free surface models LaMEM and FEMS-2D (both 4 km after 200 kyears) and LAPEX-2D (5.2 km after 2 Myears). During the following 20 Mio years vertical velocities are small (order of 0.25 cm/year). It takes a few tens of Mio years until the slab successfully detaches from the surface. Rapidly it subducts through the upper mantle and reaches the bottom of the box after some tens of Mio years. As the slab is fixed at the right side of the model box, subduction is accompanied by considerable roll back with a horizontal velocity of the order of 1 cm/year.

4.1.1. Comparison of slab shapes

First we compare the shapes of the subducting slabs. As the temporal behaviour is different (see below) we chose snapshots for stages at which the subducting slab has reached a depth of approximately 400 km. As can be seen in Fig. 4, the similar stages are reached at different times. The geometries are quite similar on first order, but a detailed examination reveals some differences: the FDCON case shows a slightly stronger thickening of the horizontal part of the plate, associated with a larger trench retreat compared to the I2ELVIS-model. In the FDCON-model the originally right angles at the edges of the slab front are less deformed than in the I2ELVIS case. The CITCOM model has already subducted to a slightly greater
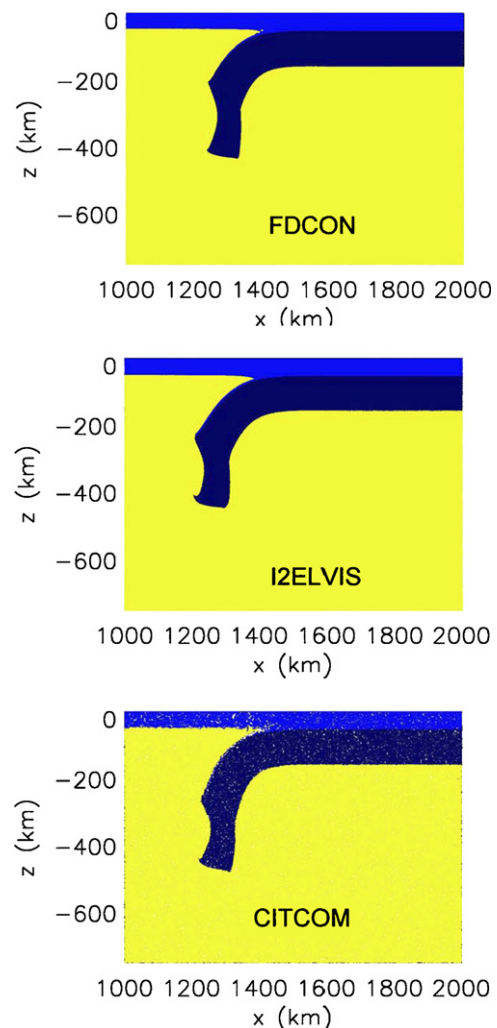

Fig. 4. Shapes of different case 1 models at similar stages: FDCON: 40 Myears, I2ELVIS: 34.7 Myears, CITCOM: 38.1 Myears. Viscosity averaging: geometric mean in all cases.

Fig. 3. Typical behaviour of a case 1 model (here FDCON-4 is shown). Streamlines are also shown.

depth than the other two models, however, the trench retreat the same as for FDCON. A careful examination of the three models shows that a thin layer of soft surface material is entrained on top of the subducting slab. As will be discussed more in detail below, this layer is thinner than the grid resolution of all of the models, thus its lubricating effect may differ from code to code. Most importantly the lubrication effect depends on the way of determining the effective viscosity in the entrainment region (see Section 3.2). All three models shown in Fig. 4 used geometric means (Eq. (8)) for viscosity averaging, that is the reason for the first order similarity of the geometries.

Fig. 5 shows the effect of viscosity averaging on the shapes of the slabs. Note that the snapshots are taken at different times, so that the slab tips have reached comparable levels. The deformation of the slab tip is strongest for the case with the harmonic mean, which yields the weakest effective viscosity, while the original shape of the rectangular slab is best preserved for the stiffer arithmetic mean case. In arithmetic case, the bending is more localized near the trench, as deeper parts of the slab have already undergone unbending during the more slowly subduction. In the harmonic ca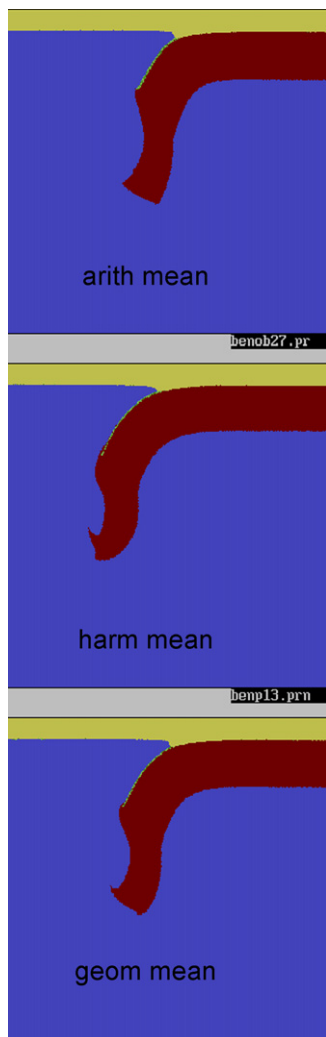ses, which are taken at shorter times, unbending has not proceeded that far. The geometric mean case shows characteristics just in between the other two cases.

4.1.2. Comparison of temporal behaviour

To compare the temporal behaviour of the different models Fig. 6 shows the depth of the slab as a function of time for different codes and highest resolutions each. Diagrams of the full set of models with different resolutions is given in the Appendix A. In contrast to the others, I2VIS and I2ELVIS also used of local refinement (curves with symbols). All models (FDCON, I2VIS, I2ELVIS, CITCOM, LAPEX2D) using geometric mean (greenish curves) lie close together and reach the 400 km depth level after 35–41 Myears. Interestingly LAPEX2D used a higher weak layer viscosity of 10^{20} Pa s instead of 10^{19} and still shows good agreement with the others who used the geometric mean.

The highest resolution uniform grid models using arithmetic mean for viscosity averaging (FDCON and I2ELVIS) (bluish curves) show a significant slower subduction. Increasing the grid resolution locally (on the expense of grid resolution far away from the trench area), I2VIS with arithmetic means (blue curve with diamonds) shows a significant faster subduction compared to the uniform grid, arithmetic mean models (blue curves) and lies close to the slowest models with geometric means (greenish curves). Averaging the viscosity near boundaries even more locally as is done by I2ELVIS (blue curve with squares) speeds up subduction even more, entering the field of curves with the geometric mean.

However, testing the harmonic mean as a third reasonable possibility shows again a dramatic effect: FDCON, I2VIS and I2ELVIS highest resolution models show (reddish curves) that subduction is now much faster than in the previous cases, even when using the highest resolutions. However, locally refined models now show the tendency towards slower subduction, these curves lie on the slower side of the set of the harmonic averaging models.

A resolution test of the models of case 1 with a weak top layer is shown in Fig. 7 which shows the time at which the slab tip passes the 400 km level as a function of the characteristic grid size used in the runs. Increasing the resolution clearly shows that the curves with the geometric or arithmetic means converge from high values towards a time between 34 and 38 Myears. The I2VIS and I2ELVIS runs with the harmonic mean show a trend of coming from small values converging towards an asymptotic value between 25 and 30 Myears. FDCON (harmonic) has the same asymptotic trend, but shows characteristic oscillations which are strongly damped as the resolution increases. The frequency of these oscillations, which are also observed for the geometric averaging models of FDCON, correlates with the frequency with which a FD-grid line coincides with the compositional interface between the lithosphere and the soft layer (non-connected crosses in Fig. 7). The convergence behaviour of FDCON with infinite norm scheme is similar to arithmetic averaging models, but the asymptotic trend is not well defined.

In Fig. 8, we show the temporal behaviour of the trench rollback evolution of our highest resolution models for different rheological averaging schemes used. Only the results of I2ELVIS and I2VIS are shown, as those allow for local grid refinement in the trench region. During the first 15–20 Myears all models with local refined grids agree well with each other and follow roughly the evolution of the uniform grid run with geometric mean. The uniform grid models with harmonic or arithmetic mean significantly differ already from the beginning. At later stages, $t > 20$ Myears, the retreat curves diverge, with the harmonic mean models retreating fastest (reddish curves) and the arithmetic mean curves retreating slowest (bluish curves). The full set of models with different resolutions is shown in Appendix A, Fig. A2a–c.
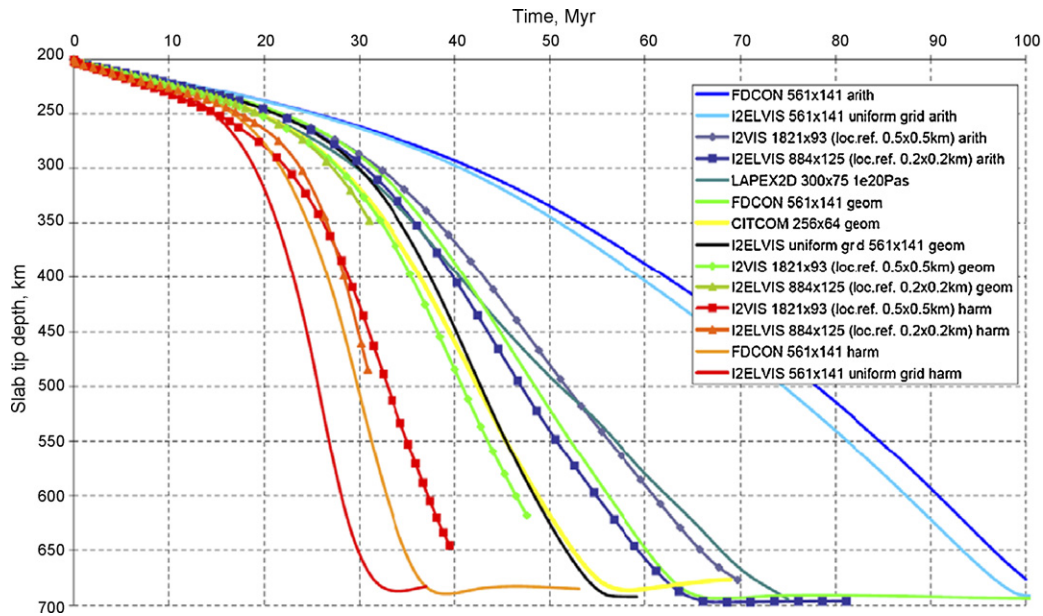

Fig. 5. Comparison of the shapes of the slabs for different viscosity averaging methods using I2VIS. Note that the snapshots are taken at different times (59.6, 24.4, 37.8 Myears from top to bottom), so that the slab tips have reached comparable levels.

Fig. 6. Temporal behaviour of case 1 modelled by different codes with highest resolutions each. Each curve shows the position of the deepest part of the slab (slab tip) as a function of time below the initial surface of the lithosphere. See the legends for the used codes and grid resolution. Note that the codes I2VIS and I2ELVIS also use local refinement at the trench area (given in parentheses in the legend). Outside the trench area the resolution decreases to 10×46 km at model sides. At the lower boundary the vertical resolution was 1 km. The rheological means (cf. Section 3.2) are denoted as geom for geometric, harm for harmonic and arith for arithmetic, respectively. In contrast to the others, LAPEX2D was run with 10^{20} Pa s for the weak layer.

From this comparison it becomes clear that the codes have some problems in correctly solving the stated fluid dynamical problem (which should have a unique solution). They only converge to roughly comparable subduction histories if the resolution is drastically increased. Harmonic and arithmetic mean runs approach the geometric solution from opposite sides, runs with geometric mean often seem to start from values closer to the asymptotic value.

Yet, extrapolation of these runs towards the exact solution is not fully satisfactory as the differences between results obtained by different viscosity averaging methods are still large, and asymptotic values of harmonic and other means do not yet coincide for the resolutions used. In the next section, we give an explanation for the diverse behaviour of our models in terms of decoupling and lubrication.
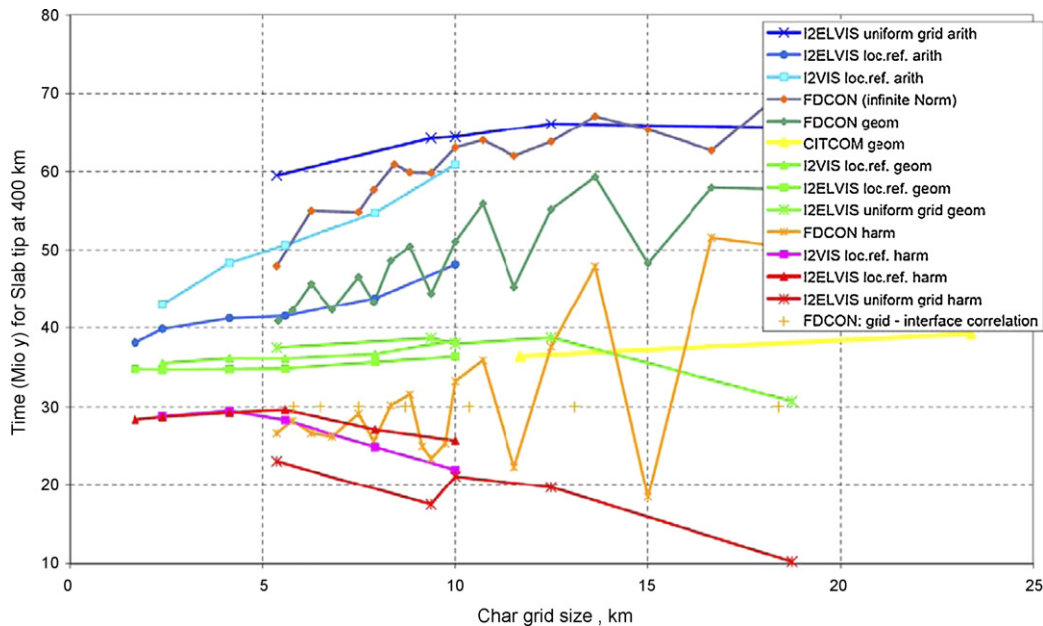

Fig. 7. Resolution test of all models of case 1. The time at which the slab tip passes the 400 km level beneath the initial lithosphere surface is shown for each model as a function of characteristic grid size. The different rheological averaging schemes are arithmetic, geometric and harmonic mean, as well as the infinite norm scheme. While for FDCON, CITCOM, and I2ELVIS (uniform grid) the characteristic grid size is equal to the actual grid size (equal in horizontal and vertical direction), the characteristic grid size of the I2VIS and I2ELVIS runs with local refinement was taken as the geometric mean of the nominal grid size (length divided by number of cells in each direction and then taking the geometric mean of the two directions) and the finest grid size within trench region (also taking the geometric mean of the two directions), scaled so that the characteristic grid size equals the nominal grid size for the coarsest resolution. The symbols "FDCON: grid-interface match" show the grid sizes at which the lithospheric surface coincides with a FD-grid line for FDCON. This sequence correlates with the oscillations seen in the "FDCON harm" and "FDCON geom"-curves.
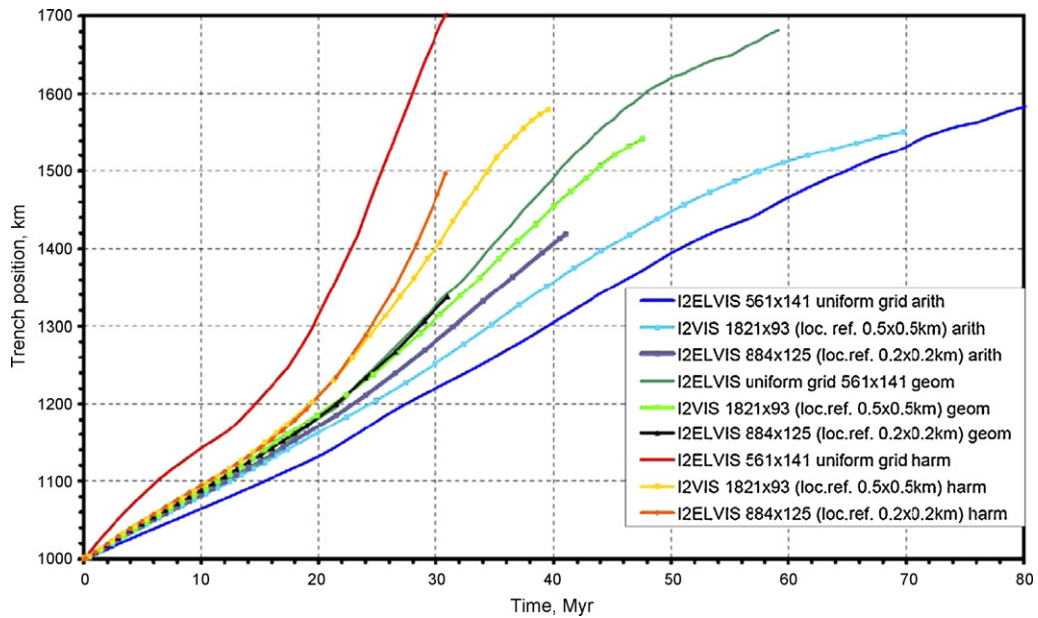
Fig. 8. Highest resolution results for trench rollback of case 1 for different rheological averaging methods (geometric, arithmetic, harmonic mean). Several runs were done with grid refinement following the moving trench. For these runs, outside the trench area the resolution decreases to 10×46 km at model sides, except for the 381×76 node model, which has uniform horizontal resolution with 5×46 km at the model sides. At the lower boundary the vertical resolution was always 1 km.

4.1.3. Decoupling from the top—the role of entrainment of weak material

In order to examine the reason for the differences among the models with different viscosity averaging, Fig. 9 presents a closer look at the details of one of our models. The marker distributions show that a thin layer of the weak surface material is entrained on top of the downgoing slab. This layer is only one to three markers wide (in this example, every 4th marker is shown in every direction), thus lies below the resolution of the FD grid. As the weak surface layer markers carry weak rheology, they decrease the effective viscosity within a layer immediate above the downgoing slab, but only irregularly within distinct FD grid cells as is visible by the irregular distribution of bluish FD cells (Fig. 9 left). This lubrication helps the subduction of the slab, however, it cannot be resolved adequately as the lubrication layer is thinner than the grid resolution. We believe that such differences in non-resolvable lubrication

behaviour is the reason for the significant differences between the models if different rheological averaging methods are used, and if the resolution is varied.

4.2. Free surface models

Case 1 has also been modeled by LAPEX2D, LaMEM and FEMS-2D assuming a free surface instead of the weak surface layer (Fig. 10). These runs point out that the results depend strongly on the numerical resolution that is employed. Low resolution is accompanied by a higher resistance of the mantle at the trench region to flow and spread on top of the sinking slab. Coarse elements do not well approximate the high curvatures at the tip of the "overrolling" mantle wedge building up near the trench and make the surface geometrically stiffer (or less flexible). This requires more strain until one of the surface elements at the tip
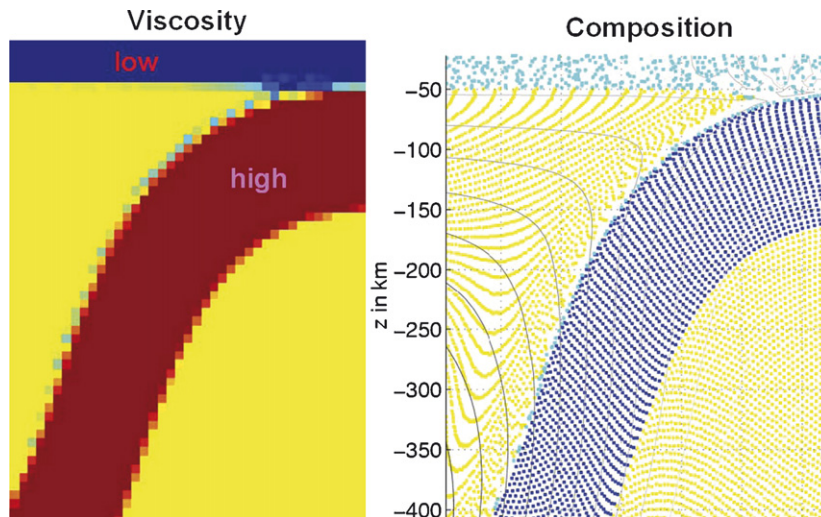

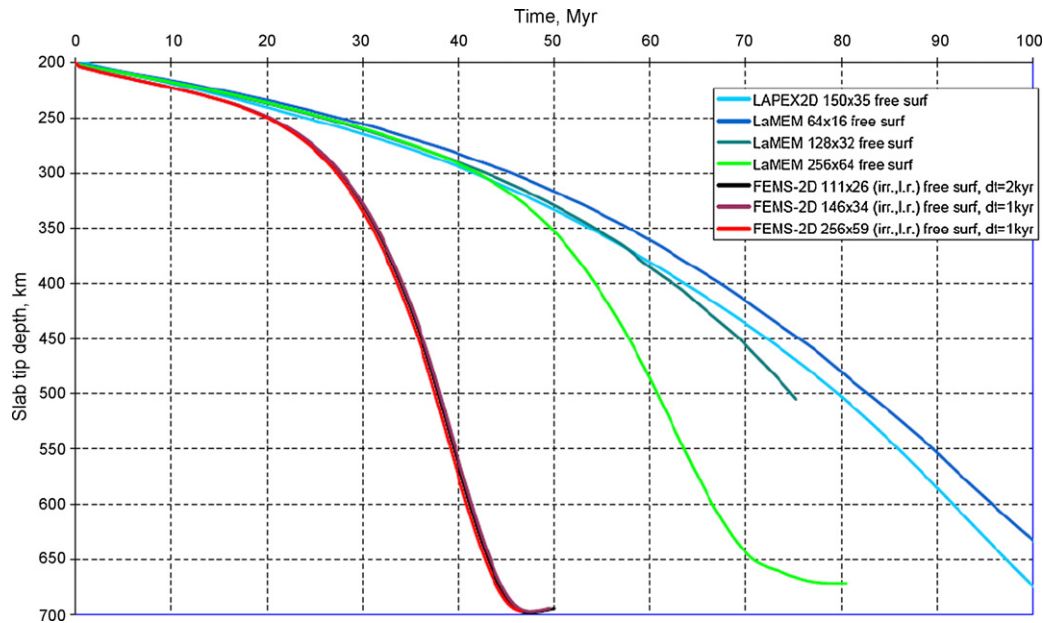**Fig. 9.** Details of the entrainment and lubrication of the soft surface layer.

Fig. 10. Comparison of temporal behaviour of case 1 models assuming a free surface instead of a weak layer. The FEMS-models used an irregular (irr.) mesh with local refinement (l.r.) near the trench, the given *x–y* grid resolution are only approximate values for comparison, calculated from the total number of nodes. The three FEMS-2D models are very similar so that the curves partly overlap.

of the wedge gets overturned and re-meshing (i.e. 'slip' of one element) is performed. Large elements cannot resolve this overturning and lead to 'numerical locking'—severe underestimation of the correct solution by the accepted numerical approximation. This numerical 'locking effect' is especially pronounced in the beginning of the slab sinking process, when the mantle wedge loading is still small. Moreover, the results in Fig. 10 show that low-resolution LaMEM and LAPEX2D runs probably demonstrate pertinent locking at the mantle wedge even at later stages of subduction. Larger velocities and full decoupling of the slab from the surface are only obtained for higher resolutions and re-meshing near the trench.

In the FEMS-2D runs an unstructured mesh with a high resolution around the slab and low resolution away from the slab has been used. Increasing the resolution in these runs mainly increased the resolution away from the slab and made the mesh more regular. As the number of markers in the marker chain specifying the slab shape was the same in the different runs, the resolution directly around the slab was nearly identical in the runs. This is the reason for almost identical curves for different resolutions. Thus, increasing the resolution in areas away from the slab does not change the results. On the other hand, the time step has some effect on the behaviour because remeshing is done once the light material becomes "overturned" while overriding the slab. Bigger time steps lead to an earlier remeshing because the light material becomes faster overturned.

Even for the highest resolutions there are still significant differences between the different codes. We believe that these differences are due to the different remeshing schemes used, particularly near the trench (see Section 3.1). However, once the decoupling reached a quasi-steady state, the subduction velocities of the FEMS-2D and LaMEM models are similar.

4.3. Models without a lubrication layer (case 2)

As has been shown in Section 4.1, the entrainment of weak material helped decoupling of the slab from the surface but did not lead

to fully converging results when using different viscosity averaging methods. Therefore, we carried out a second comparison of results (case 2 models) for a model in which the "soft layer" had the viscosity $\eta_s = 10^{21}$ Pa s, i.e. the same viscosity as the mantle. The idea was, that if any entrainment of this layer takes place there will be no lubrication between the slab and the ambient mantle. This model setup has been run with different resolutions by the codes summarized in Table 3.

4.3.1. Comparison of slab shapes and temporal behaviour

The general behaviour of this case is shown in Fig. 11. During the first 40 Myears the leading, vertical part of the slab stretches in a Rayleigh–Taylor-like fashion, while the surface part of the lithosphere stays near the original surface. Between 40 and 60 Myears the original trench part of the slab (i.e. the triple point between lithosphere, mantle and surface layer) detaches from the initial surface and starts to sink into the mantle. However, the coupling to the surface is still so strong that the deeper parts of the slab continue to further stretch and thin. Trench retreat is less efficient than in the case 1.

Table 3
Series 2 models: models with strong surface layer, $\rho_s = 0$ kg/m^3, $\eta_s = 10^{21}$ Pa s

Model name	Resolution	No. of markers	Averaging method	Remarks
FDCON-7	161×41	1800×450	Geom	
FDCON-8	241×61	2700×675	Geom	
FDCON-9	321×81	3600×900	Geom	
FDCON-10	401×101	4500×1125	Geom	
FDCON-11	561×141	6250×1570	Geom	
FDCON-12	321×81	3600×900	Harm	
FDCON-13	321×81	3600×900	Arith	
FDCON-14,15	561×141		Harm, arith	
LAPEX2D	300×75		Geom	$\rho_s = 0$ or 1000 kg/m^3
ABAQUS-mesh	300×70		Harm	
CITCOM-3	128×32		Geom	
CITCOM-4	256×64		Geom	
CITCOM-5	512×128		Geom	
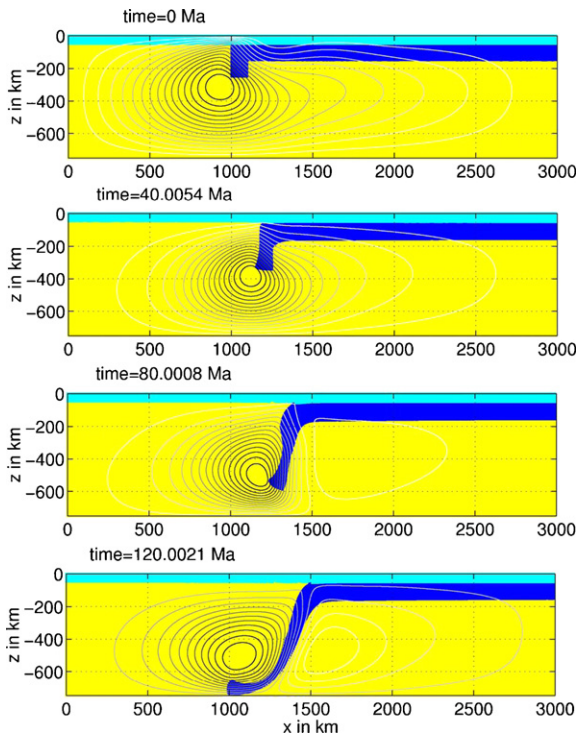
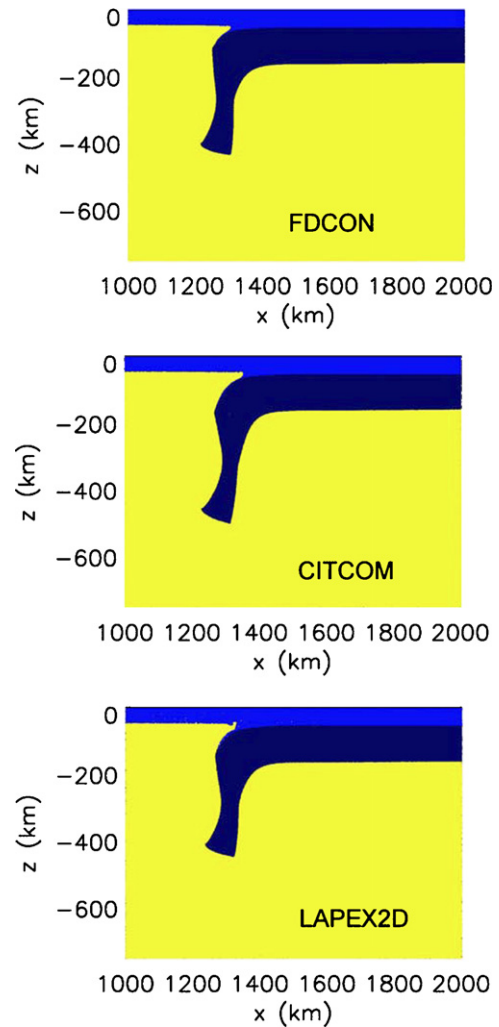Fig. 11. Typical behaviour of a case 2 model (here FDCON-11 is shown).

Fig. 12. Shapes of different case 2 models at similar stages: FDCON: 60 Myears, LAPEX2D at 60 Myears, CITCOM at 67.2 Myears. Viscosity averaging: geometric mean in all cases. LAPEX2D used $\rho_s = 1000$ kg/m^3.

Fig. 12 shows a comparison of shapes of several case 2 models run with different codes, all using the geometric mean for viscosity averaging. The snapshots have been taken around 60 Myears and the shapes are quite similar. They all agree that the deformation of the slab tip is significantly less than in case 1 models, however, the slab is more stretched than in series 1. The detachment from the surface is significantly delayed.

Fig. 13 shows the temporal behaviour of the case 2 models of our best resolution models. In contrast to the case 1 curves, subduction is significantly slower. Compared to case 1 the results fall into a narrow range of solutions. Choosing the same (here geometric) averaging scheme, the difference between the codes is small, the 400 km depth level is passed within the time interval 60–68 Myears or reach the bottom after times between 93 and 105 Myears, LaMEM and LAPEX2D lying on the slower side of the set of curves. However, inspecting curves with different rheological averaging schemes at compositional boundaries shows notable but consistent differences: Harmonic averaged models are fastest, arithmetic averaged models are slowest. As for these variances slabs reach the bottom of the box after times between 80 Myears (harmonic mean runs) and 110 Myears (arithmetic mean runs).

We now address the question about the reason for the still notable differences between the different case 2−curves of Fig. 13. They are smaller than in the case 1, however, they are surprising since no lubrication layer is involved in case 2 models. An examination of the triple point between the three different materials reveals, that using the arithmetic (stiff) mean leads to piling up of surface material near the triple point, whereas for harmonic averaging a thin layer of light surface material is entrained. Obviously piling up of light material produces sufficient buoyancy to delay subduction of the triple point, while with harmonic (soft) averaging the surface material near the boundary can more easily be smeared out. This smearing out distributes buoyancy over a wider distance allowing earlier subduction of the triple point. The role of the appropriate averaging method will be discussed below

4.4. Results of laboratory experiments and comparison with numerical models (case 3)

In this section, we present some laboratory results and compare them with numerical results obtained under the same initial conditions.

The experimental subduction process during the free sink of the lithosphere into the upper mantle is similar to what has been already described in details in previous experiments (Faccenna et al., 2001; Funiciello et al., 2003a,b, 2004). During the first phase of the experiment, the trench retreats with a fast rate that increases progressively in time with the amount of subducted material (Fig. 14). The dip of the slab also increases, reaching a maximum value of about 60°. The retrograde slab motion is always associated with a significant displacement of the mantle driven by the subducting lithosphere. Resulting mantle circulation is organized in two different components, poloidal and toroidal, both active since the beginning of the experiment (see Funiciello et al., 2006 for details).

When the leading edge of the slab approaches the bottom boundary ($t_{exp} \sim 3$ min), the slab reduces its rate of retreat and its dip by about 15° (see Fig. 14). Afterwards, the slab touches the bottom boundary and the trend of the trench retreat changes slow-
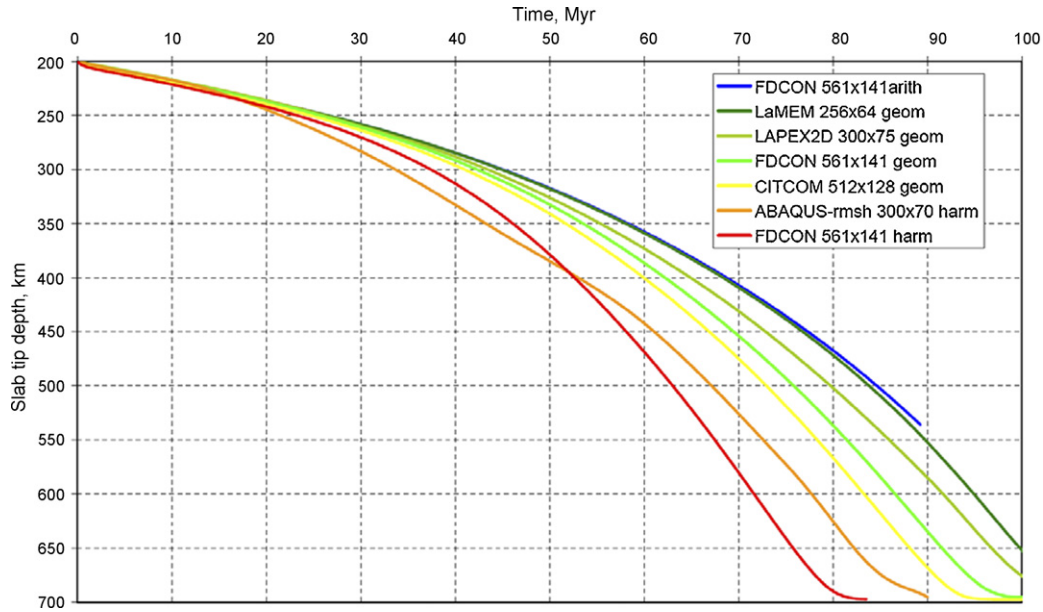
Fig. 13. Highest resolution results of different codes for slab tip depth evolution for case 2. Different viscosity averaging schemes (arithmetic, geometric and harmonic means) have been used.

ing down for about 12 min. After the interaction the trench starts to bend laterally into an arc shape allowing lateral circulation of mantle material around the slab and resuming the trench retreat. This 3D nature of the laboratory model is shown in a surface view (Fig. 15). Due to the arc shape the subduction process continues in the central part, that otherwise would be inhibited. This arcuation can create small delay of the time necessary for the slab tip near the sides to reach the bottom of the box compared to the central part of the plate. From this moment, the trench retreat velocity is approximately constant and the slab dip reaches steady state values of about 45°, while the slab tip lies horizontally on top of the analogue of the 660 discontinuity.

We now compare the laboratory results to numerical models using the same physical parameters and a similar initial configuration (cf. Fig. 2 and Table 1). To mimic the free laboratory surface the FDCON-series was run with a weak surface layer of 0.8 cm thickness, zero density and a viscosity of 3.2 Pa s (i.e. 1/10th of the mantle viscosity). These numerical experiments used the arithmetic, the geometric and harmonic mean for the calculation of the viscosity. We also performed numerical simulations with LaMEM and FEMS-2D (MILAMIN), employing a true free surface (which is however remeshed regularly).

Both the numerical free surface and the soft surface layer results with harmonic viscosity averaging show a similar sinking behaviour as the analogue model until the slab reaches the bottom (cf. Figs. 14 and 16). All models show an accelerating phase during which the slab dip increases. The bottom is first reached by the central part of the slab in the lab model after about 4 min, while the sides of the laboratory slab and the numerical slab reach

Fig. 14. Result of the laboratory experiment at 6 different times. Note that the dark visible regions represent the side view of the slab while slightly lighter parts show the central part of the slab deeper within the tank.

Fig. 15. Surface view of the laboratory model at the time 19′ 15″ illustrating the 3D effects. The brighter part of the plate on the right is still at the surface, the subducted part lies left of the arcuate trench.
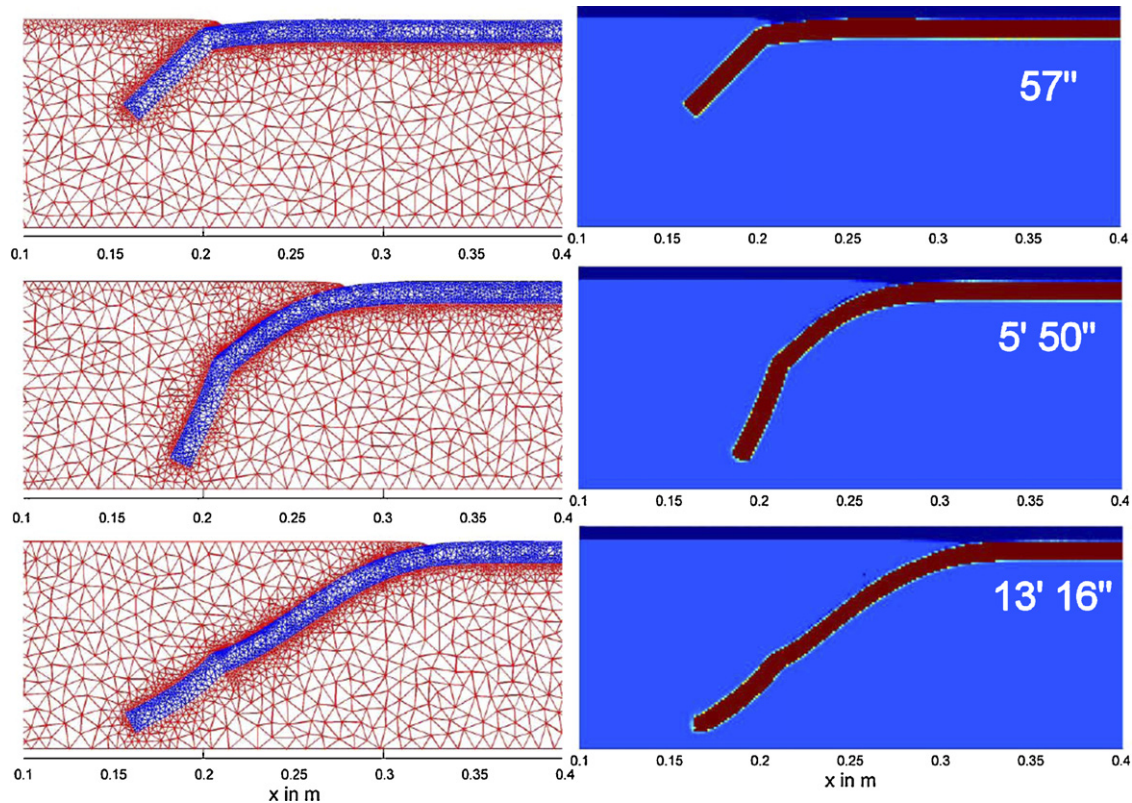
Fig. 16. Zoom in for viscosity snapshots of the FEMS-2D (left), FDCON (right) numerical models for times 57s, 5′ 50″, and 13′ 16″ which are comparable to the time steps presented for the laboratory experiment. For FDCON the harmonic mean for viscosity is used.

the bottom approximately after 6 min. As a remnant from the initial geometry, the numerical slabs still show a weak kink after 6 min. This is missing in the laboratory models, which started from a smooth initial geometry (cf. Fig. 2). The retreat of the numerical models shows a good agreement with the laboratory results until the experimental slab reaches the bottom of the experimental box (see Figs. 14 and 16). At later stages ($t > 6$ min) the laboratory model is dominated by 3D-flow structures which cannot be reproduced numerically using a 2D code. As a consequence, the amount of retreat in both models starts to diverge drastically after slab interaction with the bottom.

It is interesting to compare the development of the slab dips of the analogue experiment with the numerical model (see Figs. 14 and 16). During the early stage (2–4 min) the slab dip increases to values between 70 and 80° in the numerical model which is steeper than in the analogue model ($\sim 60°$), but then, in agreement with the laboratory model, decreases to a value of about 45° approaching the bottom boundary (around 5–6 min).

A significant difference also arises in the deflection (horizontal flattening) of the slab after it reaches the bottom boundary. The analogue slab shows a quite large horizontal flattening at late stages whereas the numerical slab flattens out only negligibly. We explain this difference again by the 2D confinement of the sublithospheric mantle material on the right-hand side of the numerical slab: Flattening of the front part of the slab in the lab model is accompanied by progressive trench retreat, and thus requires considerable decrease in mantle volume beneath the retreating slab. While this mass flux is achieved by 3D flow in the lab model, the 2D confinement of the numerical model does not allow this mantle region, captured by the slab, to decrease in volume. As a result, the late stage of the numerical model is

characterized by a straight, gently dipping slab, whose dip angle only changes slowly with time as the trench slowly migrates to the right.

Figs. 17 and 18 show the temporal behaviour of the depth of the slab tip and of the position of the retreating trench, respectively. Note that the starting position of the numerical and the laboratory models are slightly different due to the slight differences in initial geometry (curvature of the leading part of the slab). Generally, the free surface numerical results are in good agreement with the laboratory experiments, if a resolution of at least 256×64 nodes is employed or local mesh refinement near the trench is used. Smaller resolutions result in much slower subduction rates. An examination of the numerical results revealed that the critical part of the free surface simulation is the formation of a cusp-like triple point, i.e. the trench, above the subducting slab. Once this point has been formed, the mantle 'overflows' the subducting slab in a fairly steady manner. If the triple point cannot be resolved, due to for example insufficient resolution, a more oscillatory behaviour is observed which results in drastically slower rates of subduction.

It is interesting to note that the numerical results using the arithmetic and geometric mean differ dramatically (for FDCON) or considerably (for I2ELVIS) from the experimental results in both retreat and slab tip depth (see Figs. 17 and 18). These slabs are also slightly to significantly slower than the runs with harmonic mean. The best agreement between the laboratory and numerical models is obtained with the harmonic mean – models (Fig. 17a) and with harmonic or geometric mean –models with local refinement (Fig. 17b) during the first 200–300 s. During this time, which is characterized by progressive slab bending and trench retreat, the best numerical models consistently show
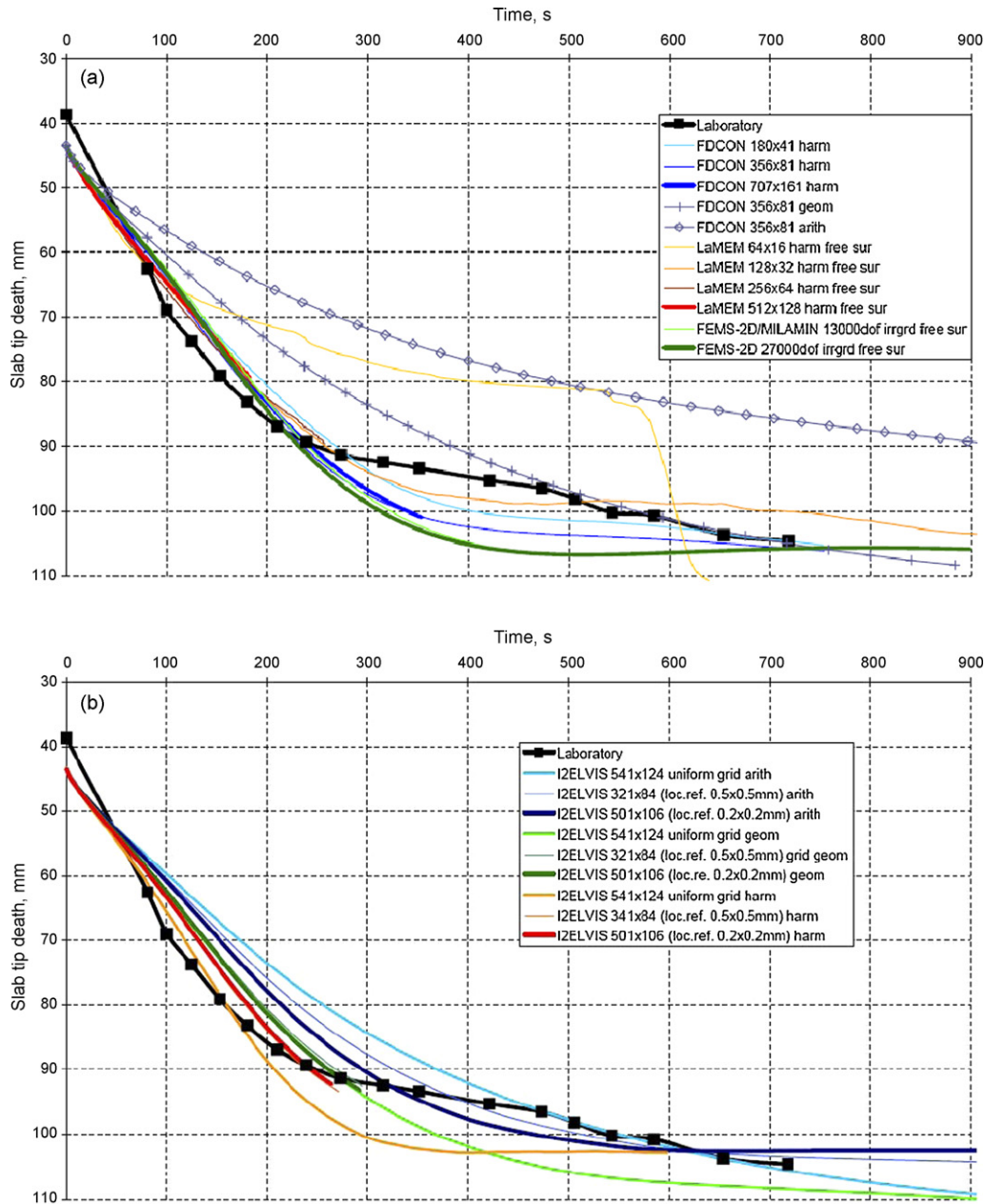
Fig. 17. (a) Comparison between laboratory and numerical slab tip depths obtained by the codes FDCON, LaMEM and FEMS-2D. FDCON used a viscosity of the soft surface layer equal to 1/10 of the mantle viscosity. (b) As (a) but for I2ELVIS, using a viscosity of the soft surface layer of 1/100 of the mantle viscosity.

a slightly slower sinking velocity of the slab tip, and a slightly higher retreat velocity compared to the lab model. As the differences are small we cannot distinguish whether they are due to small errors in material properties (e.g. 20% uncertainty in the determination of silicone putty or glucose syrup viscosity), differences in initial geometry or unaccounted effects such as surface tension. After 300 s the laboratory slab tip depth (which is determined as an average along the visible leading edge, cf. Fig. 14) increases slower than the numerical ones. We explain this difference as being due to the 3D-flow structure of the laboratory model. After 200–300 s the numerical trench retreat is faster than the retreat of the laboratory model. Again, this may be due to the 3D-flow structure associated with a arcuate shape of the trench. Later ($t > 1200$ s) trench migration of the numerical models decreases due to 2D confinement, while the increasing 3D-flow contribu-

tion of the laboratory model allows a slight speed up of trench migration.

We may summarize this comparison by stating that the first, 2D-dominated stage of the laboratory slab could be well reproduced by numerical models which either have a free surface and sufficient resolution (at least 256×64 nodes) or which simulate the free surface by a weak zero-density layer and take the harmonic viscosity averaging. Later, 3D effects accelerate the trench retreat, decelerate slab sinking, and lead to a flattening of the subducted slab, a feature which in principle cannot be reproduced by 2D numerical models. Finally, it should be noted that, given sufficient resolution and using the harmonic mean, the free surface models and the soft surface layer models (both with 1/10 and 1/100 of the mantle viscosity) show a high degree of agreement.
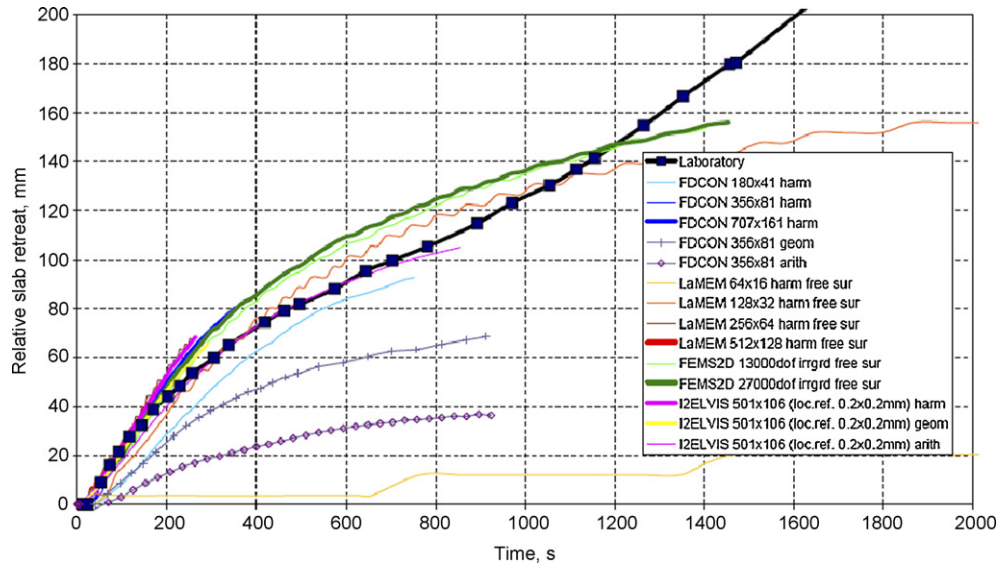
Fig. 18. Comparison between experimental and numerical relative slab retreat.

5. Discussion

5.1. The problem of viscosity averaging at compositional boundaries

5.1.1. The physical meaning of the different averaging laws

One important result of this work is the extremely strong effect of the viscosity averaging scheme applied to regions which contain compositional boundaries (cf. Section 3.2). Here we provide a physical explanation of these different methods. As illustrated in Fig. 19, the harmonic mean of two viscosities is equivalent to taking the effective viscosity of a rheological model with two viscous elements in series. Such a model correctly describes the volume-averaged deformation of a channel flow containing a flow-parallel compositional interface, i.e. undergoing simple shear. It corresponds to a weak effective viscosity. Thus, in any fluid dynamical setup with compositional boundaries an effective viscosity based on harmonic means will be realized in those local regions in which the compositional interface is undergoing interface-parallel shearing. On the other hand, if the viscous stress at the interface is characterized by pure shear, the effective viscosity of this configuration is given by a rheological model with two viscous elements in parallel, i.e. the arithmetic mean. Such a model correctly describes the volume-averaged stress of a region containing a compositional interface undergoing interface-parallel pure shear. This model corresponds to a stiff effective viscosity. Thus, for all slab regions undergoing interface-parallel pure shear, the arithmetic mean is the appropriate averaging method.

A realistic slab is expected to contain interface sections which are both under simple and pure shear, thus its net behaviour will lie between these two cases. However, interface-parallel simple shear may be dominant in several circumstances: (a) near the trench the flow in the cusp-like wedge may be approximated by a simple corner flow. For low angle corner flow it can be shown that interface-parallel simple shear is dominant within the flow and at the interface to the slab. (b) In case of a large viscosity contrast between slab and overriding mantle, the low viscous region might "see" the high viscous region as a rigid interface in first approximation. Due to the incompressibility condition ($\vec{\nabla} \cdot \vec{v} = 0$) normal deviatoric stresses in the low viscous region drop to 0 near a rigid boundary in a local coordinate system parallel to the interface, while tangential shear stresses do not.

For these reasons, the harmonic mean is suggested to be more appropriate for high viscosity contrasts such as 10^4 and flows dominated by cusp-like overriding wedges, as is also evident from the comparison of the laboratory and numerical results (Section 4.4).

5.1.2. Apparent shift of rheological boundaries, "2D-Stokes flow"

Fig. 20 illustrates, that the geometric mean lies in the middle between the arithmetic and harmonic mean. A Finite Difference or Finite Element cell lying on the interface will essentially have a stiff effective viscosity if the arithmetic mean is used, or a weak effective viscosity if the harmonic mean is used. Alternatively, its viscosity will be of intermediate order of magnitude (arithmetic mean of $\log_{10}$-viscosity) if the geometric mean is used. There is no simple rheological model for the geometric mean. As a result of this consideration, a model with arithmetic mean apparently shifts the rheological boundary into the weak region, while the harmonic mean shifts the boundary into the stiff medium. We explain the behaviour of case 2 models by this effect: in the arithmetic mean case the critical triple point at the trench is part of the effectively stiff region, the formation of a cusp is impeded, and subduction is delayed, while in the harmonic mean case it is part of the weak region, and subduction is facilitated.
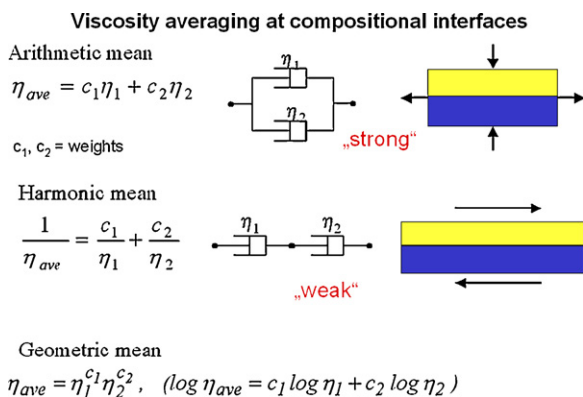

Viscosity averaging at compositional interfaces

Arithmetic mean

$$\eta_{ave} = c_1 \eta_1 + c_2 \eta_2$$

c_1, c_2 = weights

"strong"

Harmonic mean

$$\frac{1}{\eta_{ave}} = \frac{c_1}{\eta_1} + \frac{c_2}{\eta_2}$$

"weak"

Geometric mean

$$\eta_{ave} = \eta_1^{c_1} \eta_2^{c_2}, \quad (\log \eta_{ave} = c_1 \log \eta_1 + c_2 \log \eta_2)$$

Fig. 19. Illustration of the physical meaning of the different averaging methods.
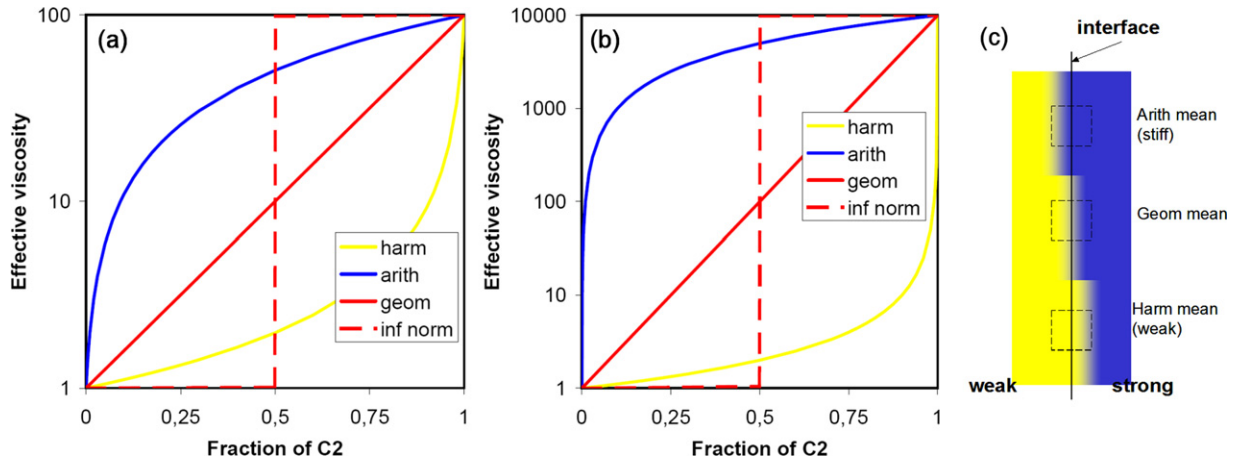
Fig. 20. Effective viscosity of one numerical cell in a Eulerian formulation depending on the fraction of material 2 for the different averaging methods for a viscosity contrast 100 (a) and 10,000 (b). (c) Depending on the averaging method, the effective position of the interface is shifted towards the stiff or weak material.

For comparison, the infinite norm average (cf. Eq. (9)) is also shown (Fig. 20a and b, dashed). This scheme can be regarded as a zero order approximation of the harmonic mean for $C_2 < 0.5$, changing to a zero order approximation of the arithmetic mean for $C_2 > 0.5$. Thus, the apparent shift of the rheological boundary into either the strong or the weak region along a macroscopically large section of the compositional boundary is expected to be statistically balanced at sufficiently high resolution.

Fig. 20a and especially b illustrates that care has to be taken when using the different averaging schemes. For example, already a very minor fraction of C_2-material present in a numerical cell may increase its effective viscosity dramatically, if arithmetic means are taken, or, conversely, a very minor fraction of C_1-material present in a numerical cell may decrease its effective viscosity dramatically, if harmonic means are taken. While these effects are still consistent with fluid dynamics if these numerical cells experience pure shear or simple shear deformation, respectively, spurious effects may arise for arbitrary deformation configurations, and higher grid resolutions or more sophisticated rheology schemes are required.

On the other hand, a careful consideration of choosing an appropriate averaging scheme may allow to obtain reasonable results even for cases in which features such as a cusp-like triple point separating regions with strong viscosity contrasts, or a thin lubrication layer as in the case 1 models are not well resolved by the FD or FE grids. While at coarse resolution such a layer has no effect on lubrication when taking the arithmetic or geometric averaging, harmonic averaging effectively accounts for the lubrication viscosity.

We have tested and confirmed this conclusion by carrying out resolution tests with 2D-circular shaped bodies ("2D-Stokes flow") of different density with and without a surrounding lubrication layer moving in a viscous medium (Fig. 21a and b, respectively). For this test we used FDCON. As long as the grid size is larger than the lubrication layer, the arithmetic and geometric means model do not "see" the lubrication layer and seem to converge to almost the same asymptotic value, while the harmonic means models converge towards a significantly different value. As the grid resolution becomes fine enough to see the lubrication layer, the slopes of resolution curves of the arithmetic and geometric mean change and converge towards the same value as the harmonic mean models. Thus, for a simple body surrounded by a lubrication layer the harmonic mean provides an appropriate averaging scheme, and coarse resolution models are already closer to the asymptotic value than the other averaging schemes. The convergence behaviour of the infinite norm scheme lies somewhere between the convergence

behaviour of the arithmetic and geometric means (as already seen in the convergence test of case 1), i.e. it requires a very high resolution to reasonably account for the lubrication layer.

Similar resolution tests for circular bodies without lubrication layer ("2D-Stokes flow") have been carried out (Fig. 21b). For a highly viscous body all four means show a well-behaved convergence behaviour towards the same asymptotic velocity even for coarse resolution, but they start from different distances to the
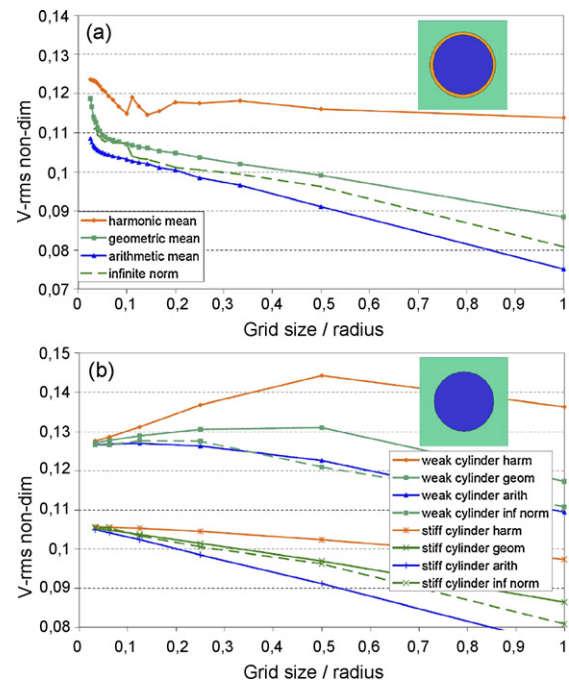

Fig. 21. (a) Resolution test, using FDCON, for a circular body of different density, surrounded by a weak lubrication layer, using the harmonic, arithmetic, geometric or infinite norm mean for viscosity averaging near boundaries. The circular body has a density contrast $\Delta\rho$ with respect to the background material, a viscosity 10^2 times higher then the background viscosity η_0 and is situated in the centre of a square box which has a height 10 times the radius r_0. Boundary condition at the box sides is free slip. The circular body is surrounded by a lubrication layer of thickness 5% of the radius, a viscosity of 10^{-2} the background viscosity and has the same density as the background material. The ordinate shows the root-mean-square velocity within the whole box, scaled by $\Delta\rho g r_0^2 / \eta_0$. (b) Resolution tests for a stiff and weak circular body of different density without lubrication layer (i.e. 2D-Stokes flow). Same setup and scaling as in (a). The stiff cylinder has a viscosity of $100\eta_0$, the weak cylinder of $0.01\eta_0$.

asymptotic value. For a weak viscous body the different schemes converge monotonically only for resolutions better than about 0.3 (grid size/radius). Comparing the different schemes shows that, at same resolution, a low viscous sphere is best approximated by using the arithmetic, geometric, or infinite norm scheme, while a highly viscous sphere in a low viscous medium is best approximated by using the harmonic mean. In the latter case all four means converge towards the asymptotic value from below. This general convergence behaviour for a 2D-Stokes flow has also been verified by another code (ABAQUS). Therefore, we conclude that the above statements are generally valid, and only details of the convergence paths will depend on the numerical schemes.

5.1.3. Which averaging scheme is to be preferred?

What can we learn from these considerations? From Fig. 19 we conjecture that an appropriate way of averaging at an inter-face would be to switch between arithmetic and harmonic mean depending on the local state of stress and strain rate at the interface. Numerically this is somewhat cumbersome. Our resolution tests with models with moderate viscosity contrast (two orders of magnitude) demonstrate, that the arithmetic and geometric means seem to converge from below towards a subduction rate, which, however, is still slower than the asymptotic value from harmonic mean models. We therefore have to leave it open whether for case 1 type models we suggest the harmonic or geometric mean as the most appropriate scheme. If the viscosity contrasts are higher (four orders of magnitude) our case 3 models show that harmonic averaging converges satisfactorily and agrees best with the lab model results and with free surface models. If detached highly viscous bodies with or without lubrication layers are studied, preference to the harmonic mean is suggested by the "2D-Stokes flow" resolution tests. Similar conclusions were reached in a study by Deubelbeiss and Kaus (this volume), in which the accuracy of various finite
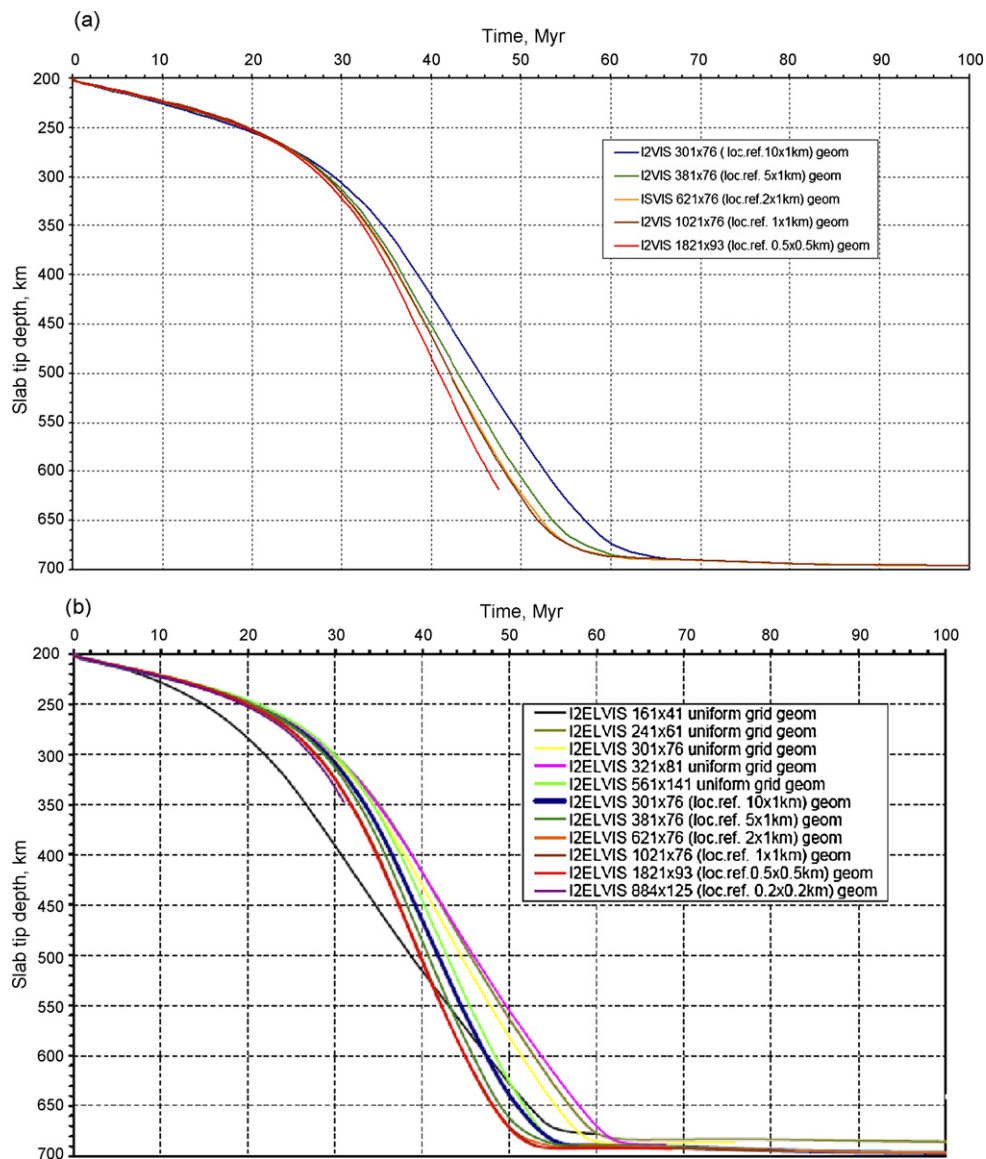

Fig. A1. Temporal behaviour of case 1 modelled by different codes and with different resolution. Each diagram shows the position of the deepest part of the slab (slab tip) as a function of time below the initial surface of the lithosphere. See the legends for the used codes and grid resolution. Note that the codes I2VIS and I2ELVIS (a and b) use local refinement at the trench area (given in parentheses in the legend). Outside the trench area the resolution decreases to 10×46 km at model sides, except for the 381×76 node model, which has uniform horizontal resolution with 5×46 km at the model sides. At the lower boundary the vertical resolution was always 1 km. The rheological means (cf. Section 3.2) are denoted as geom for geometric, harm for harmonic and arith for arithmetic, respectively. In contrast to the others, LAPEX2D (Fig. A1e) was run with 10^{20} Pa s for the weak layer.
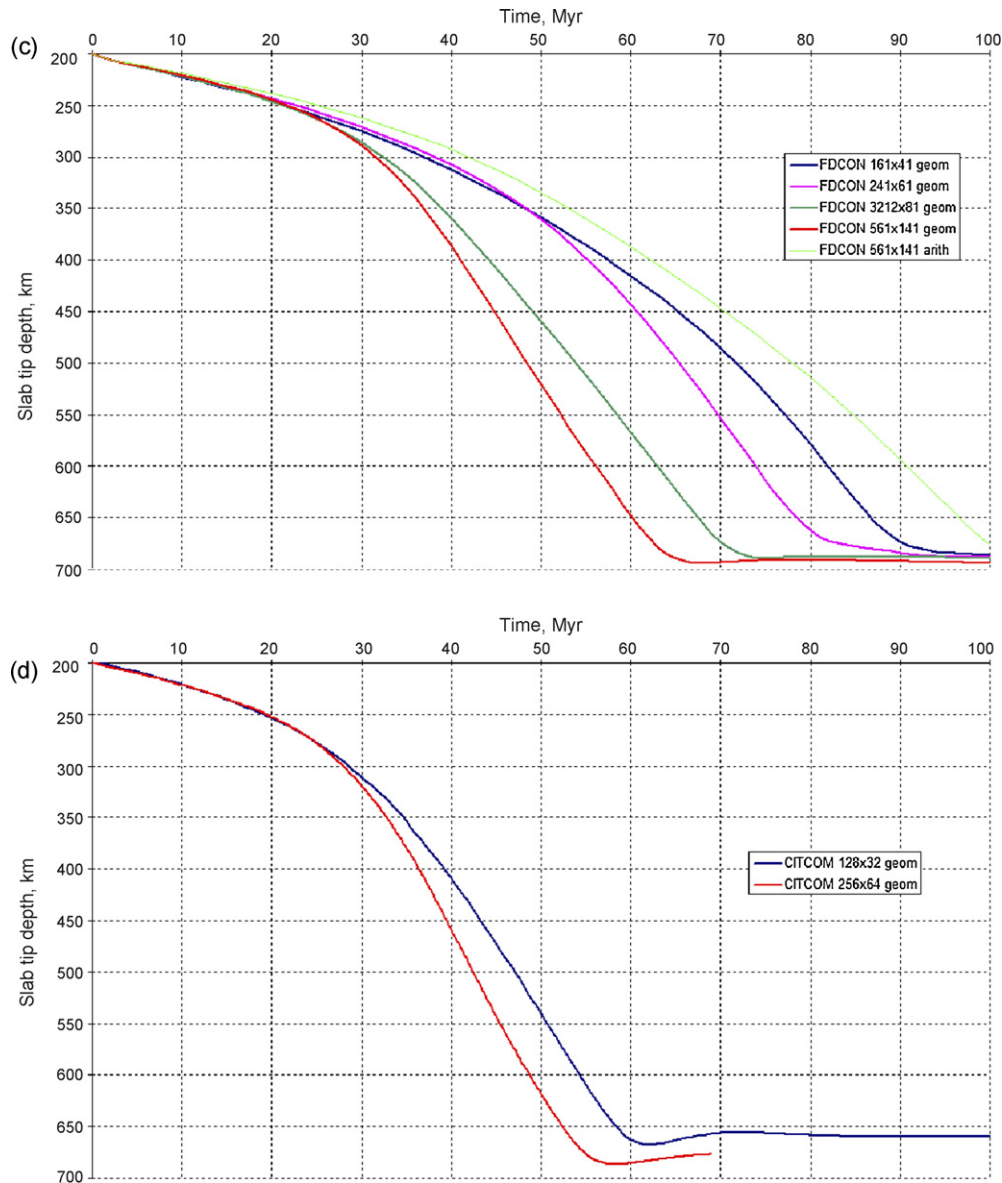
Fig. A1. (*Continued*)

difference and finite elements methods were compared with analytical solutions.

It should, however, be noted, that in any case the different means have to converge to the same asymptotic behaviour. Preference of one or the other scheme just gives better results at coarser resolution. For a simple Stokes flow with a lubrication layer and for case 3 our models show that convergence can be reached, for our case 1 and case 2 models our models came only close to convergent results.

5.2. Simulating a free surface

Obviously a free surface plays an important role in subduction: It produces a topography step of the order of 4 km at the trench. As the overriding material (viscous mantle in our numerical and laboratory cases) deforms and spreads on top of the slab it aids the bending and downgoing of the highly viscous slab.

Comparing the cases with the soft layer (Fig. 6) with the free surface models (Fig. 10) suggests that not all approaches have fully

converged, but that the temporal subduction behaviour tends to become quite similar for increasing resolution: the 400 km levels is reached after 25–38 Myears by the highest resolution models with a soft layer (Fig. 7), while it is reached by the free surface models around 33 Myears. Given the present uncertainties these numbers are regarded to be in good agreement.

Thus, assuming a zero-density weak zone to mimic a free surface has been shown to be a reasonably good approach, surprisingly, even a highly viscous zero-density layer does a relatively good job (case 2). However, we encountered practical problems with this approach: as consequence of the weak surface layer approach the subduction of the triple point (between slab, overriding mantle and surface layer) always drags down a thin layer of surface material. While this effect is fluid dynamically consistent, its lubrication effect has no physical equivalence in models with a real free surface. However, if free surface codes invoke a local remeshing scheme which moves the triple point along the surface of the subducting slab (cf. LaMEM and FEMS-2D, Section 3.1), this localized stick–slip behaviour may be regarded as an equivalent to trench lubrication
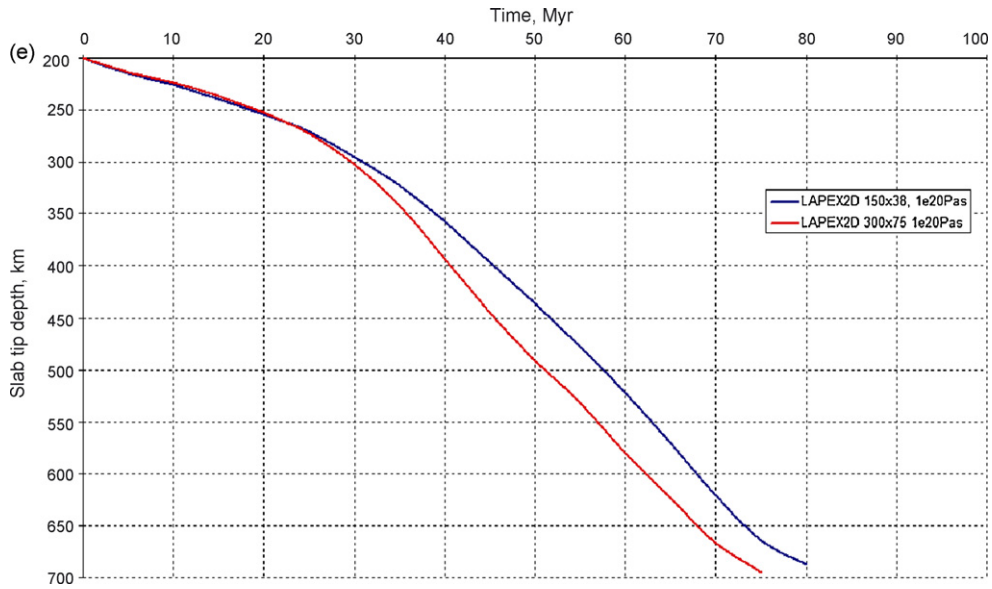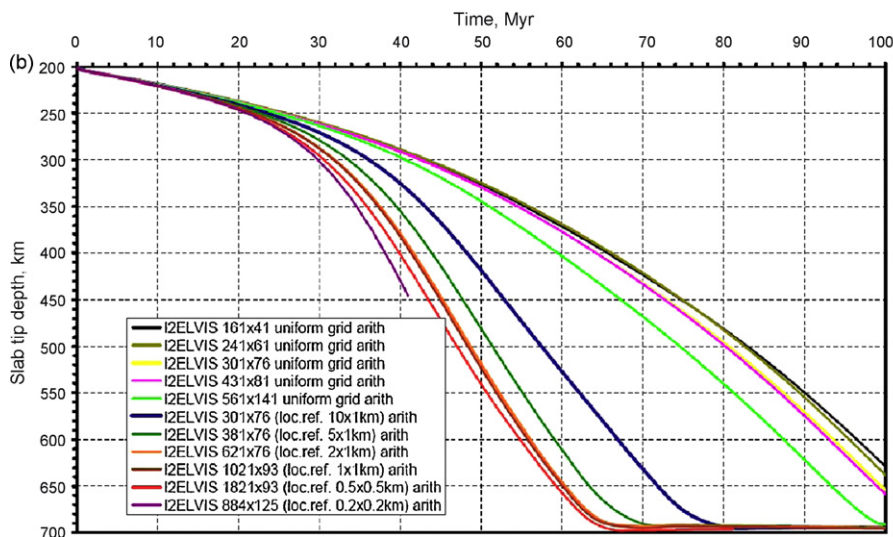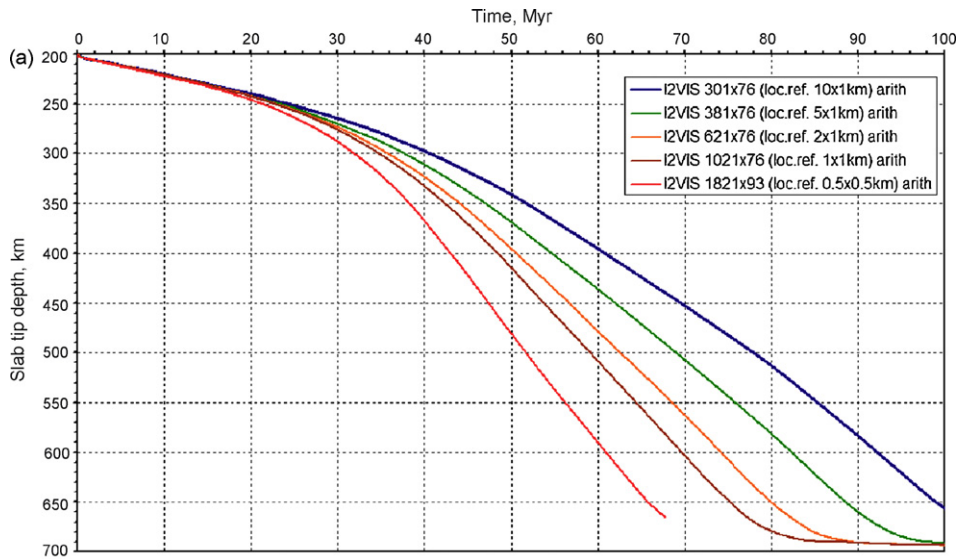
Fig. A1. (*Continued*).

Fig. A2. Comparison of temporal behaviour of case 1 for models with different rheological averaging and different resolution. Else as Fig. A1.

as present in the soft surface layer models. The importance of this lubrication effect at greater depth seems to be minor in comparison with the decoupling effect close to the trench. This can be inferred from comparing the models with the weak layer with the free surface models (Figs. 6 and 10): the free surface models are only marginally slower compared to the highest resolutions models with a soft-top layer. The difference lies within the present numerical uncertainty, but if it is due the lubrication between slab and mantle at greater depth, then this effect can be regarded as being of minor importance. A possible way to test the role of entrainment of the weak zero-density material would be to allow entrainment and decoupling near the trench, but to switch off this effect (both density and weak viscosity) by transferring those markers into lithosphere markers. Although this procedure violates conservation of composition and mass, this violation is usually negligible as the entrained layer is very thin. This procedure has successful been used by Gerya and Yuen (2003b).

On the other hand, entrainment and subduction of a weak lubrication layer might have some geophysical significance. Upon

subduction water rich oceanic crust or sediments may produce a several km thick weak serpenthenized subduction channel on top of the subducting slab (e.g. Gerya et al., 2002; Gerya and Yuen, 2003b), similar to our lubrication layer. Thus coincidently, the side effect of mimicking a free surface by a weak layer might indeed lead to a rheologically reasonable scenario.

5.3. Role of viscoelasticity

As the present subduction benchmark study is based on purely viscous rheology, the question arises whether the effect of viscoelasticity might be important. A complete rheological treatment embedding elasticity cannot in general be yet embedded in a large scale subduction model, being unclear if elastic stored energy might allow the localization of deformation at a smaller scale then the resolutions today accessible. It is however possible to test the effect of a mean-field elastic stress by some of the codes benchmarked in this paper. Using the "Abaqus + remeshing" setup, a Maxwell body viscoelastic rheology has been tested, varying Young
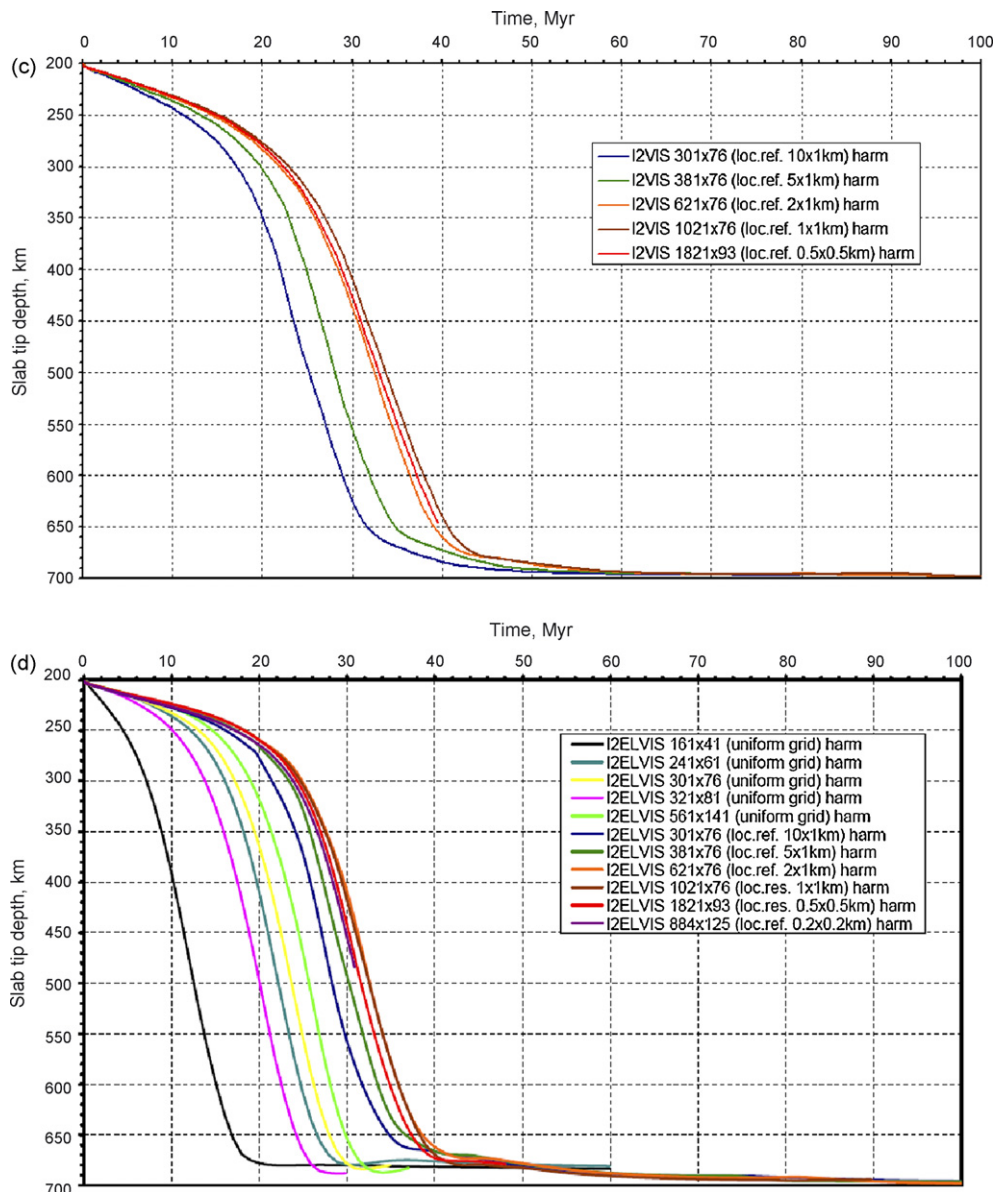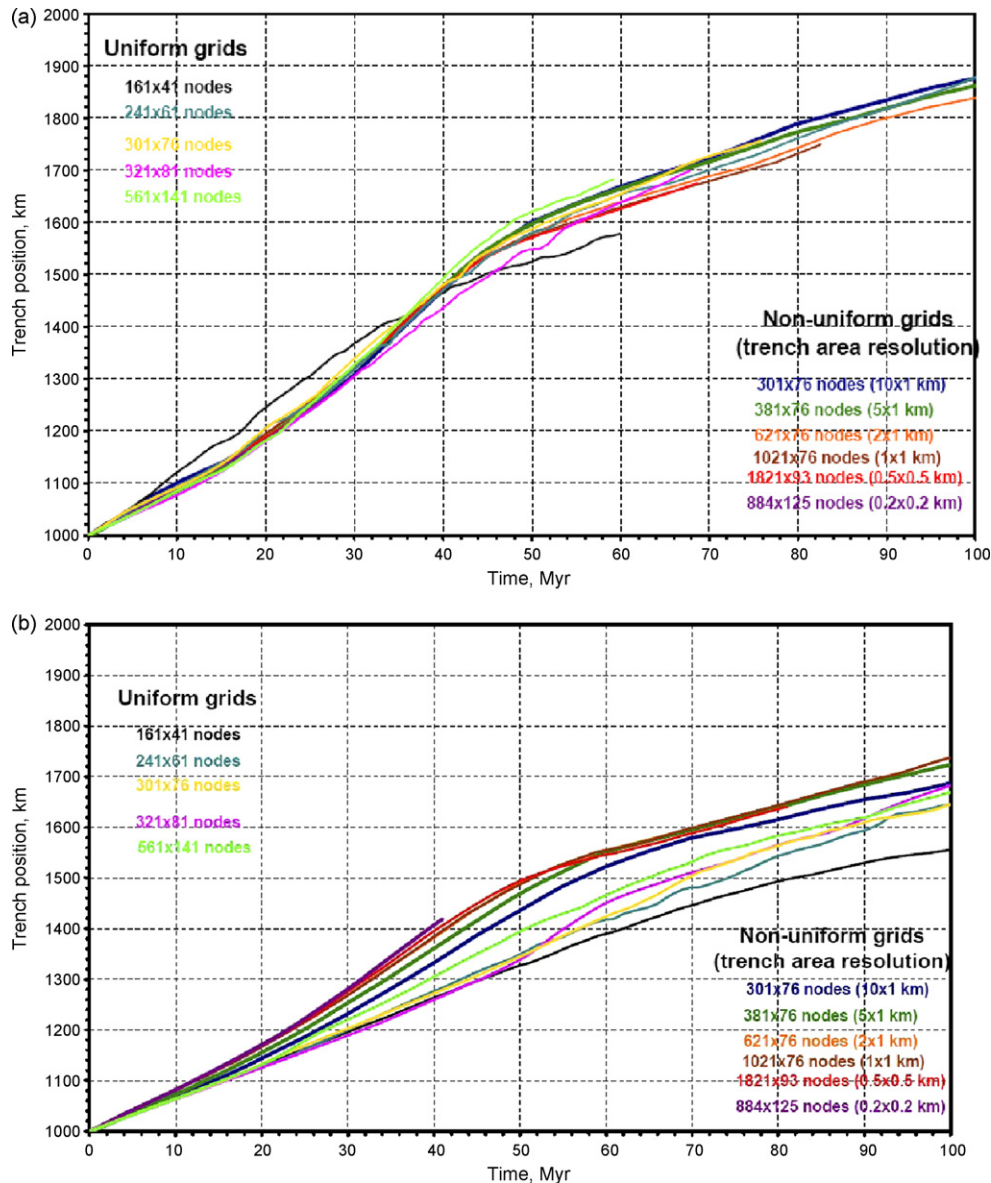

Fig. A2. (Continued).

Fig. A3. Trench rollback of case 1 for different rheological averaging methods using I2ELVIS: (a) geometric mean, (b) arithmetic mean, (c) harmonic mean. Several runs were done with grid refinement following the moving trench. In these runs, outside the trench area the resolution decreases to 10 × 46 km at model sides, except for the 381 × 76 node model, which has uniform horizontal resolution with 5 × 46 km at the model sides. At the lower boundary the vertical resolution was always 1 km.

modulus for several lithospheric viscosity profiles, to test if the addition of Earth-like elastic parameters would alter the obtained results. We find that the results are not altered by viscoelasticity for the viscous parameters defined in case 1. The viscosity of the central core part of the lithosphere has to be increased to 10^{24} or 10^{25} Pa s to see some effect of viscoelasticity assuming a reasonable Young's modulus. The detailed models can be found in Appendix B.

6. Conclusions

In conclusion, using a variety of different numerical codes and one laboratory model, we benchmark a rather simple isothermal, purely viscous spontaneous subduction setup. This setup either assumes a free surface or mimics a free surface by adding a weak, zero-density layer on top of the subduction model. The conclusions may be summarized as follows:

1. Comparing the results of these two numerical and one laboratory approaches shows that adding a weak zero-density layer on top of a numerical subduction model satisfactorily catches the important effect of a fully free surface, however, care has to be taken:

2. The effect of including this surface layer may result in severe resolution problems. We attribute these problems to be due to specific rheological averaging schemes used by the different codes. When increasing resolution the models of our different codes almost converged for cases 1 and 2, full convergence being beyond the present grid resolution. Satisfactory convergence was observed in case 3, which was characterized by a higher viscosity contrast between slab and mantle.

3. When modelling the free surface by including a weak zero-density layer, entrainment of this weak layer forms a lubrication layer on top of the subducting slab, which helps to decouple the slab from the surface. This lubrication is most important for effective subduction if present in a region close to the trench. In
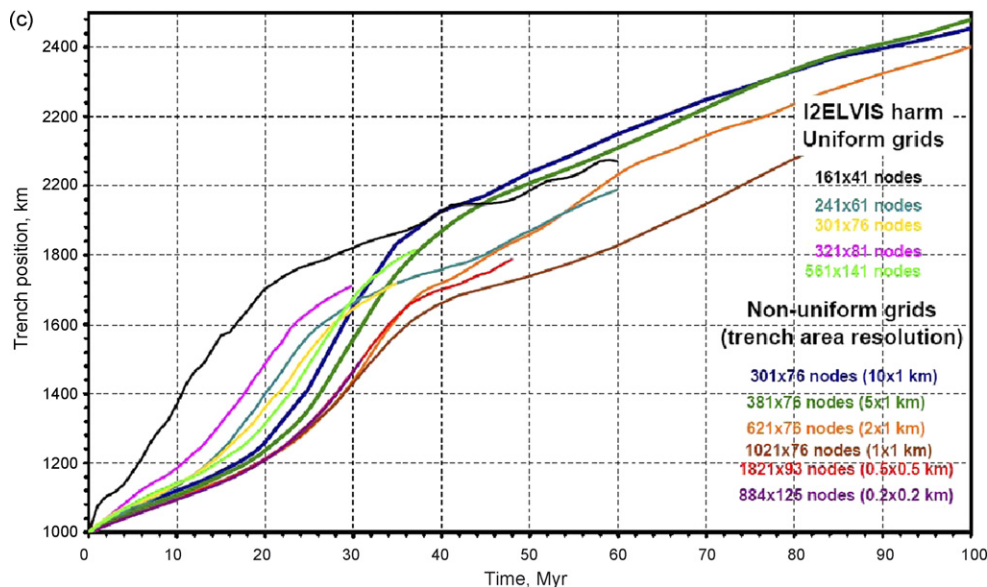
Fig. A3. (*Continued*).

reality the lubrication layer might represent a weak subduction channel.

4. Case 2 models avoid this weakening effect by assigning a high viscosity to the zero-density layer. Surprisingly, even without the lubrication layer full convergence was difficult to achieve, when different rheological schemes are used. We attribute this effect to the role of the triple point between slab, overriding mantle and surface, in particular to the impeded formation of a cusp between slab and overriding mantle.

5. For some cases (resolutions) dramatically different results are produced, depending on the viscosity averaging scheme used at rheological interfaces. Usually, harmonic averaging gives fast subduction models, arithmetic averaging gives slowly subducting slabs, and geometric averaging gives results in between. Resolution tests for case 1 suggest, that these three averaging schemes converge to a common behaviour. Models with geometric or harmonic mean seem to lie closest to the asymptotic behaviour.

6. Comparing free surface laboratory results with numerical models shows that good agreement is obtained between the two approaches if the numerical code with a free surface has sufficient resolution at the trench. If an Eulerian numerical code is employed, in which the free surface is approximated with a weak layer, harmonic averaging yields similarly good results.

7. Few tests with an infinite norm scheme for determining viscosity at grid points near a rheological boundary show that the convergence behaviour lies roughly between that of arithmetic or geometric averaging schemes.

In conclusion, our case studies provide an extensive set of tests for different approaches to model a free surface at subduction zone environments and for different rheological averaging schemes. It suggests which scheme to be used under which circumstances, and will provide a practical guide for future studies of fully dynamic subduction systems with large viscosity contrasts at compositional boundaries.

Appendix A

This appendix summarizes the results for cases 1 and 2 for various resolutions as obtained by the different codes. Both, slab tip depth and trench retreat is shown as a function of time in Figs. A1–A4. The codes, resolutions and averaging schemes used are given in the legends.

Appendix B

The effect of elasticity in a Maxwell body is usually described by the Maxwell time, defined as the ratio between viscosity and Young's modulus. Viscosity values for the lithosphere vary between 10^{21} and 10^{25} Pa s. Assuming a Young's modulus between 10^{10} and 10^{11} Pa (as constrained from seismic models), the Maxwell time for such lithosphere is in the range 10^{10} s (300 years) to 10^{15} s (30 Myears). The product of the strain rate and the Maxwell time is called Deborah number (*De*) and defines whether elasticity will dominate the solution (*De* > 10), will partially influence the solution (0.1 < *De* < 10) or does not play a role (*De* < 0.1).

As the lithospheric viscosity in this benchmark is 10^{23} Pa s, the corresponding maximum Maxwell time is on the order of 10^{13} s (300 kyears). Given that strain rates over 10^{-14} s^{-1} are usually not observed in the lithosphere, most probably *De* < 0.1, and a direct effect of elasticity is not predicted. In order to verify this, a simulation with much higher Young's modulus (10^{13} Pa) and same viscosity profile was performed (Fig. B1a) without observing any effect, confirming that in this benchmark elasticity would probably play no role. Finally, to counodeck that elasticity would play a role in the presence of higher viscosity, a simulation identical to the benchmark setup, but with the addition of a 30 km thick highly viscous (10^{25} Pa s) core in the centre of the slab, was performed with a Young's modulus of 10^{11} and 10^{13} Pa. In this setup, results are visibly different: the viscoelastic model is faster, being less dissipative, which is in agreement with a recent study (Kaus and Becker, 2007). Similar conclusions about influence of
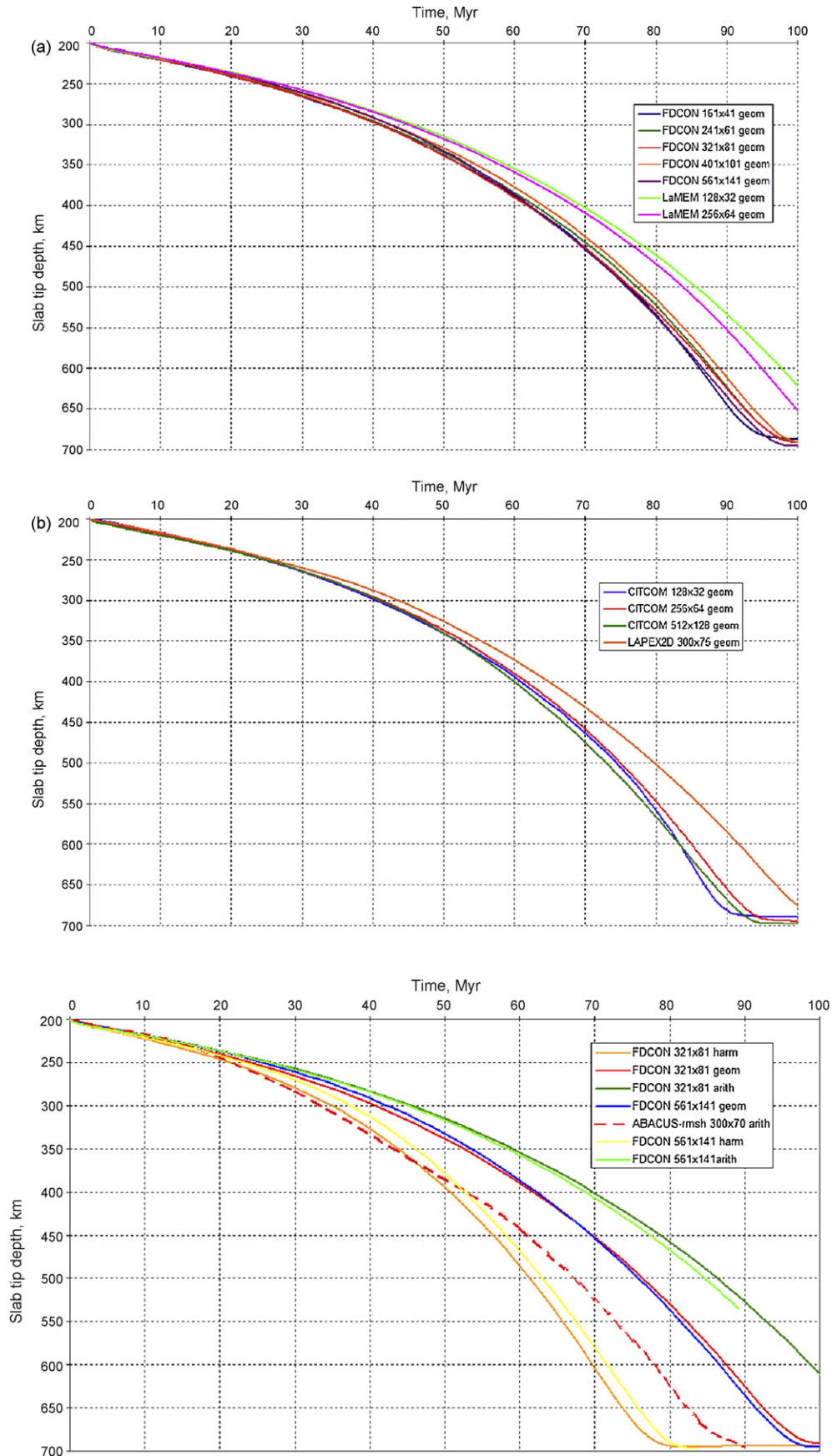
Fig. A4. Slab tip depth curves for case 2 for different codes and with different resolutions. (a) Resolution test for FDCON and LaMEM models with geometric mean. (b) Resolution test for CITCOM models, one LAPEX2D model added. (c) comparison of curves with different viscosity averaging schemes.
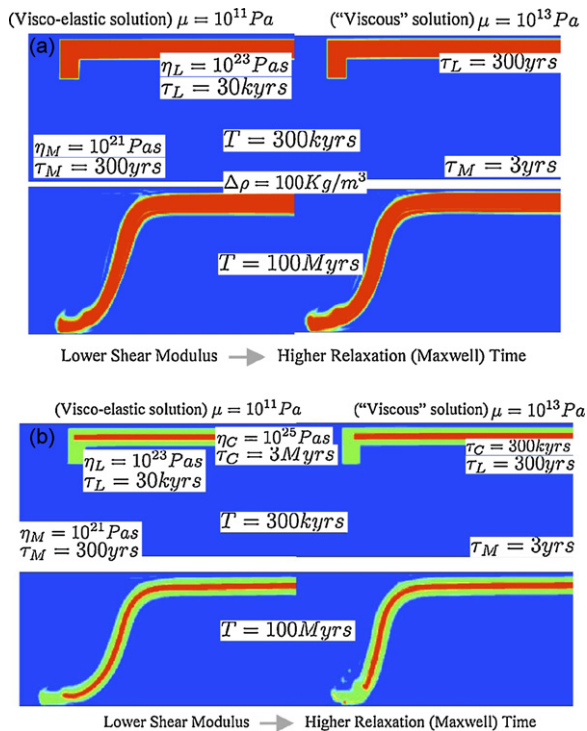
Fig. B1. (a) Test of case 1 with viscoelastic theology (Young's modulus 10^{11} Pa). (b) Modification of previous model by adding a highly viscous core in the lithosphere and increasing the Young's modulus to 10^{13} Pa.

viscoelasticity were also obtained with the viscoelastoplastic code I2ELVIS by comparing viscous solution for the setup shown in Fig. 1 with two viscoelastic experiments of identical resolution employing 6.7×10^{10} Pa and 10^{10} Pa shear modulus for all materials.

References

Babeyko, A.Yu., Sobolev, S.V., Trumbull, R.B., Oncken, O., Lavier, L.L., 2002. Numerical models of crustal-scale convection and partial melting beneath the Altiplano-Puna plateau: Earth. Planet. Sci. Lett. 199, 373–388.

Bathe, K.-J., 1996. Finite Element Procedures. Prentice Hall, Upper Saddle River, New Jersey.

Becker, T.W., Faccenna, C., Giardini, D., O'Connell, R., 1999. The development of slabs in the upper mantle: insights from numerical and laboratory experiments. J. Geophys. Res. 104, 15207–15226.

Bellahsen, N., Faccenna, C., Funiciello, F., 2005. Dynamics of subduction and plate motion in laboratory experiments: Insights into the "plate tectonics" behavior of the Earth J. Res. 110 (B1), B01401.

Buttles, J., Olson, P., 1998. A laboratory model of subduction zone anisotropy. Earth Planet. Sci. Lett. 164 (1–2), 245–262.

Capitanio, F.A., Morra, G., Goes, S., 2007. Dynamics models of downgoing plate-buoyancy driven subduction: Subduction motion and energy dissipation. Earth Planet. Sci. Lett. 262, 284–297.

Cundall, P.A., Board, M., 1988. A microcomputer program for modelling large-strain plasticity problems. In: Swoboda, G. (Ed.), 6th Interna-tional Conference in Numerical Methods in Geomechanics. A. A. Balkema, Brookfield, Vt., pp. 2101–2108.

Cuvelier, C., Segal, A., van Steenhoven, A.A., 1986. Finite element methods and the Navier–Stokes equations. D. Reidel Publishing Company, 536 pp.

Dabrowski, M., Krotkiewski, M., Schmid, D.W., 2008. MILAMIN: MATLAB-based finite element method solver for large problems. Geochem. Geophys. Geosyst. 9, Q04030, doi:10.1029/2007GC001719.

Davy, P., Cobbold, P.R., 1991. Experiments of a 4-layer continental lithosphere. Tectonophysics 188, 1–25.

Deubelbeiss, Y., Kaus, B.J.P., this volume. Comparison of Eulerian and Lagrangian numerical techniques for the Stokes equations in the presence of strongly varying viscosity. Phys. Earth Planet. Inter.

Faccenna, C., Funiciello, F., Giardini, D., Lucente, P., 2001. Episodic back-arc extension during restricted mantle convection in the central mediterranean. Earth Planet. Sci. Lett. 187 (1–2), 105–116.

Frehner, M., Schmalholz, S.M., 2006. Numerical simulations of parasitic folding in multilayers. J. Struct. Geol. 28 (9), 1647–1657.

Funiciello, F., Morra, G., Regenauer-Lieb, K., Giardini, D., 2003a. Dynamics of retreating slabs. I. Insights from two-dimensional numerical experiments. J. Geophys. Res. 108, 2206, doi:10.1029/2001JB000898 (reprint vorhanden, Subduction ordner).

Funiciello, F., Faccenna, C., Giardini, D., Regenauer-Lieb, K., 2003b. Dynamics of retreating slabs. II. Insights from three-dimensional laboratory experiments. J. Geophys. Res. 108, 2207, doi:10.1029/2001JB000896.

Funiciello, F., Faccenna, C., Giardini, D., 2004. Role of lateral mantle flow in the evolution of subduction systems: insights from laboratory experiments. Geophys. J. Int. 157, 1393–1406.

Funiciello, F., Moroni, M., Piromallo, C., Faccenna, C., Cenedese, A., Bui, H.A., 2006. Mapping the flow during retreating subduction: laboratory models analyzed by Feature Tracking. J.Geophys. Res. 111, B03402, doi:03410.01029/02005JB003792.

Gerya, T.V., Yuen, D.A., 2003a. Characteristics-based marker-in-cell method with conservative finite-differences schemes for modeling geological flows with strongly variable transport properties. Phys. Earth Planet. Inter. 140, 295–320.

Gerya, T.V., Yuen, D.A., 2003b. Rayleigh–Taylor instabilities from hydration and melting propel 'cold plumes' at subduction zones. Earth Planet. Sci. Lett. 212, 47–62.

Gerya, T.V., Stöckhert, B., Perchuk, A.L., 2002. Exhumation of high-pressure metamorphic rocks in a subduction channel—a numerical simulation. Tectonics 21 (1056), 6-1–6-19.

Gerya, T.V., Yuen, D.A., 2007. Robust characteristics method for modeling multiphase visco-elasto-plastic thermo-mechanical problems. Phys. Earth Planet. Inter. 163, 83–105.

Griffiths, R.W., Turner, J.S., 1988. Folding of viscous plumes impinging on a density or viscosity interface. Geophys. J. 95, 397–419.

Griffiths, R.W., Hackney, R.I., Vanderhilst, R.D., 1995. A laboratory investigation of effects of trench migration on the descent of subducted slabs. Earth Planet. Sci. Lett. 133 (1–2), 1–17.

Guillou-Frottier, L., Buttles, J., Olson, P., 1995. Laboratory experiments on structure of subducted lithosphere. Earth Planet. Sci. Lett. 133, 19–34.

Hughes, T., 1987. The Finite Element Method. Dover Publications, Mineola, New York.

Jacoby, W.R., 1976. Paraffin model experiment of plate tectonics. Tectonophysics 35, 103–113.

Jacoby, W.R., Schmeling, H., 1982. On the effects of the lithosphere on mantle convection and evolution. Phys. Earth Planet. Inter. 29, 305–319.

Kaus, B.J.P., Becker, T.W., 2007. Effects of elasticity on the Rayleigh–Taylor instability: implications for large-scale geodynamics. Geophys. J. Int. 168, 843–862, doi:10.1111/j.1365-246X.2006.03201.x.

Kincaid, C., Olson, P., 1987. An experimental study of subduction and slab migration. J. Geophys. Res. 92, 13832–13840.

Kincaid, C., Griffiths, R.W., 2003. Laboratory models of the thermal evolution of the mantle during rollback subduction. Nature 425, 58–62.

Martinod, J., Funiciello, F., Faccenna, C., Labanieh, S., Regard, V., 2005. Dynamical effects of subducting ridges: insights from 3-D laboratory models. Geophys. J. Int. 163 (3), 1137–1150.

Moresi, L., Solomatov, V.S., 1995. Numerical investigation of 2D convection with extremely large viscosity variations. Phys. Fluids 7 (9), 2154–2162.

Moresi, L., Gurnis, M., 1996. Constraints on the lateral strength of slabs from three-dimensional dynamic flow models. EPSL 138, 15–28.

Poliakov, A.N., Cundall, P.A., Podladchikov, Y.Y., Lyakhovsky, V.A., 1993. An explicit inertial method for the simulation of the viscoelastic flow: an evaluation of elastic effects on diapiric flow in two- and three-layers models. In: Stone, D.B., Runcorn, S.K. (Eds.), Flow and Creep in the Solar System: Observations, Modelling and Theory. Kluwer Academic Publishers, pp. 175–195.

Schellart, W.P., 2004a. Kinematics of subduction and subduction-induced flow in the upper mantle. J. Geophys. Res. 109 (B7), B07401, doi:10.1029/2004JB002970.

Schellart, W.P., 2004b. Quantifying the net slab pull force as a driving mechanism for plate tectonics. Geophys. Res. Lett. 31, L07611, doi:10.1029/2004GL019528.

Schellart, W.P., 2005. Influence of the subducting plate velocity on the geometry of the slab and migration of the subduction hinge. Earth Planet. Sci. Lett. 231, 197–219.

Schellart, W.P., Freeman, J., Stegman, D.R., 2007. Evolution and diversity of subduction zones controlled by slab width. Nature 446 (March (7133)), 308–311.

Schmalholz, S.M., 2006. Scaled amplification equation: a key to the folding history of buckled viscous single-layers. Tectonophysics 419 (1–4), 41–53.

Schmeling, H., Jacoby, W.R., 1981. On modelling the lithosphere in mantle convection with non-linear rheology. J. Geophys. 50, 89–100.

Schmeling, H., Marquart, G., 1991. The influence of second-scale convection on the thickness of the continental lithosphere and crust. Tectonophysics 189, 281–306.

Schmeling, H., Monz, R., Rubie, D.C., 1999. The influence of olivine metastability on the dynamics of subduction. Earth Planet. Sci. Lett. 165, 55–66.

Shemenda, A.I., Grocholsky, A.L., 1992. Physical modelling of lithosphere subduction in collision zones. Tectonophysics 216, 273–290.

Shewchuk, J.R., 1996. Engineering a 2D quality mesh generator and delaunay triangulator. In: Manocha, M.C.L.a.D. (Ed.), Applied Computational Geometry: Towards Geometric Engineering. Lecture Notes in Computer Science. Springer-Verlag, pp. 203–222.

Stegman, D.R., Freeman, J., Schellart, W.P., Moresi, L., May, D., 2006. Influence of trench width on subduction hinge retreat rates in 3-D models of slab rollback. Geochem. Geophys. Geosyst. 7, Q03012, doi:10.1029/2005GC001056.

Sulsky, D., Zhou, S.-J., Schreyer, H.L., 1995. Application of a particle-in-cell method to solid mechanics. Comput. Phys. Commun. 87, 236–252.

Tetzlaff, M., Schmeling, H., 2000. The influence of olivine metastability on deep subduction of oceanic lithosphere. Phys. Earth Planet. Inter. 120, 29–38.

van Keken, P., King, S., Schmeling, H., Christensen, U., Neumeister, D., Doin, M.-P., 1997. A comparison of methods for the modeling of thermochemical convection. J. Geophys. Res. 102, 22477–22495.

Weijermars, R., Schmeling, H., 1986. Scaling of Newtonian and non-Newtonian fluid dynamics without inertia for quantitative modelling of rock flow due to gravity (including the concept of rheological similarity). Phys. Earth Planet. Inter. 43, 316–330.

Weinberg, R.F., Schmeling, H., 1992. Polydiapirs: multiwave length gravity structures. J. Struct. Geol. 14, 425–436.

Zhong, S., Zuber, M.T., Moresi, L., Gurnis, M., 2000. Role of temperature-dependent viscosity and surface plates in spherical shell models of mantle convection. JGR 105 (B8), 11063–11082.